A&A, 685, A74 (2024)
https://doi.org/10.1051/0004-6361/202348244

Astronomy & Astrophysics

PDRs4All

III. JWST's NIR spectroscopic view of the Orion Bar★

Els Peeters[1,2,3], Emilie Habart[4], Olivier Berné[5], Ameek Sidhu[1,2], Ryan Chown[1,2], Dries Van De Putte[6], Boris Trahin[4], Ilane Schroetter[5], Amélie Canin[5], Felipe Alarcón[7], Bethany Schefter[1,2], Baria Khan[1], Sofia Pasquini[1], Alexander G. G. M. Tielens[8,9], Mark G. Wolfire[9], Emmanuel Dartois[10], Javier R. Goicoechea[11], Alexandros Maragkoudakis[12], Takashi Onaka[13,14], Marc W. Pound[9], Sílvia Vicente[15], Alain Abergel[4], Edwin A. Bergin[7], Jeronimo Bernard-Salas[16,17], Christiaan Boersma[12], Emeric Bron[18], Jan Cami[1,2,3], Sara Cuadrado[11], Daniel Dicken[19], Meriem Elyajouri[4], Asunción Fuente[20], Karl D. Gordon[6,21], Lina Issa[5], Christine Joblin[5], Olga Kannavou[4], Ozan Lacinbala[22], David Languignon[18], Romane Le Gal[23,24], Raphael Meshaka[4,18], Yoko Okada[25], Massimo Robberto[6,26], Markus Röllig[27,28], Thiébaut Schirmer[4,29], Benoit Tabone[4], Marion Zannese[4], Isabel Aleman[30,31,32], Louis Allamandola[12,33], Rebecca Auchettl[34], Giuseppe Antonio Baratta[35], Salma Bejaoui[12], Partha P. Bera[12,33], John H. Black[29], Francois Boulanger[36], Jordy Bouwman[37,38,39], Bernhard Brandl[8,40], Philippe Brechignac[10], Sandra Brünken[41], Mridusmita Buragohain[42], Andrew Burkhardt[43], Alessandra Candian[44], Stéphanie Cazaux[45], Jose Cernicharo[11], Marin Chabot[46], Shubhadip Chakraborty[47,48], Jason Champion[5], Sean W. J. Colgan[12], Ilsa R. Cooke[49], Audrey Coutens[5], Nick L. J. Cox[16,17], Karine Demyk[5], Jennifer Donovan Meyer[50], Sacha Foschino[5], Pedro García-Lario[51], Maryvonne Gerin[52], Carl A. Gottlieb[53], Pierre Guillard[54,55], Antoine Gusdorf[36,52], Patrick Hartigan[56], Jinhua He[57,58,98], Eric Herbst[59], Liv Hornekaer[60], Cornelia Jäger[61], Eduardo Janot-Pacheco[62], Michael Kaufman[63], Sarah Kendrew[64], Maria S. Kirsanova[65], Pamela Klaassen[19], Sun Kwok[66], Álvaro Labiano[67], Thomas S.-Y. Lai[68], Timothy J. Lee[12,†], Bertrand Lefloch[69], Franck Le Petit[18], Aigen Li[70], Hendrik Linz[71], Cameron J. Mackie[72,73], Suzanne C. Madden[74], Joëlle Mascetti[75], Brett A. McGuire[50,76], Pablo Merino[77], Elisabetta R. Micelotta[78], Karl Misselt[79], Jon A. Morse[80], Giacomo Mulas[99,5], Naslim Neelamkodan[81], Ryou Ohsawa[82], Roberta Paladini[68], Maria Elisabetta Palumbo[35], Amit Pathak[83], Yvonne J. Pendleton[84], Annemieke Petrignani[85], Thomas Pino[10], Elena Puga[64], Naseem Rangwala[12], Mathias Rapacioli[86], Alessandra Ricca[12,3], Julia Roman-Duval[6], Joseph Roser[3,12], Evelyne Roueff[18], Gaël Rouillé[61], Farid Salama[12], Dinalva A. Sales[87], Karin Sandstrom[88], Peter Sarre[89], Ella Sciamma-O'Brien[12], Kris Sellgren[90], Sachindev S. Shenoy[91], David Teyssier[51], Richard D. Thomas[92], Aditya Togi[93], Laurent Verstraete[4], Adolf N. Witt[94], Alwyn Wootten[50], Nathalie Ysard[4], Henning Zettergren[92], Yong Zhang[95], Ziwei E. Zhang[96], and Junfeng Zhen[97]

(Affiliations can be found after the references)

Received 12 October 2023 / Accepted 22 December 2023

ABSTRACT

Context. JWST has taken the sharpest and most sensitive infrared (IR) spectral imaging observations ever of the Orion Bar photodissociation region (PDR), which is part of the nearest massive star-forming region the Orion Nebula, and often considered to be the 'prototypical' strongly illuminated PDR.

Aims. We investigate the impact of radiative feedback from massive stars on their natal cloud and focus on the transition from the H II region to the atomic PDR – crossing the ionisation front (IF) –, and the subsequent transition to the molecular PDR – crossing the dissociation front (DF). Given the prevalence of PDRs in the interstellar medium and their dominant contribution to IR radiation, understanding the response of the PDR gas to far-ultraviolet (FUV) photons and the associated physical and chemical processes is fundamental to our understanding of star and planet formation and for the interpretation of any unresolved PDR as seen by JWST.

Methods. We used high-resolution near-IR integral field spectroscopic data from NIRSpec on JWST to observe the Orion Bar PDR as part of the PDRs4All JWST Early Release Science programme. We constructed a 3″ × 25″ spatio-spectral mosaic covering 0.97–5.27 μm at a spectral resolution R of ∼2700 and an angular resolution of 0.075″–0.173″. To study the properties of key regions captured in this mosaic, we extracted five template spectra in apertures centred on the three H_2 dissociation fronts, the atomic PDR, and the H II region. This wealth of detailed spatial-spectral information was analysed in terms of variations in the physical conditions–incident UV field, density, and temperature – of the PDR gas.

★ Full Table 3, a table with line intensities for the five template spectra (Table B.1), and the five template spectra are available at the CDS via anonymous ftp to cdsarc.cds.unistra.fr (130.79.128.5) or via https://cdsarc.cds.unistra.fr/viz-bin/cat/J/A+A/685/A74

† Tim Lee sadly passed away on Nov. 3 2022.

Results. The NIRSpec data reveal a forest of lines including, but not limited to, He I, H I, and C I recombination lines; ionic lines (e.g. Fe III and Fe II); O I and N I fluorescence lines; aromatic infrared bands (AIBs, including aromatic CH, aliphatic CH, and their CD counterparts); pure rotational and ro-vibrational lines from H_2; and ro-vibrational lines from HD, CO, and CH^+, with most of them having been detected for the first time towards a PDR. Their spatial distribution resolves the H and He ionisation structure in the Huygens region, gives insight into the geometry of the Bar, and confirms the large-scale stratification of PDRs. In addition, we observed numerous smaller-scale structures whose typical size decreases with distance from θ^1 Ori C and IR lines from C I , if solely arising from radiative recombination and cascade, reveal very high gas temperatures (a few 1000 K) consistent with the hot irradiated surface of small-scale dense clumps inside the PDR. The morphology of the Bar, in particular that of the H_2 lines, reveals multiple prominent filaments that exhibit different characteristics. This leaves the impression of a 'terraced' transition from the predominantly atomic surface region to the CO-rich molecular zone deeper in. We attribute the different characteristics of the H_2 filaments to their varying depth into the PDR and, in some cases, not reaching the C^+/C/CO transition. These observations thus reveal what local conditions are required to drive the physical and chemical processes needed to explain the different characteristics of the DFs and the photochemical evolution of the AIB carriers.
Conclusions. This study showcases the discovery space created by JWST to further our understanding of the impact radiation from young stars has on their natal molecular cloud and proto-planetary disk, which touches on star and planet formation as well as galaxy evolution.

Keywords: techniques: spectroscopic – HII regions – photon-dominated region (PDR) – infrared: ISM – ISM: individual objects: Orion Bar

1. Introduction

Massive stars output enormous amounts of radiative and mechanical energy into the interstellar medium (ISM) during their main sequence lifetimes. This energy injection shapes the global properties of the ISM, such as its structure, thermal balance, chemistry, and ionisation state. Negative stellar feedback plays a critical role in secular galaxy evolution as it suppresses star formation (Williams & McKee 1997; Hopkins et al. 2012; Kim et al. 2013), while positive stellar feedback results in swept-up gas and dust from which future stars can form (e.g. Elmegreen & Lada 1977; Preibisch & Zinnecker 1999; Koenig et al. 2008; Kirsanova et al. 2008; Ojha et al. 2011; Egorov et al. 2014, 2017).

This radiative and mechanical feedback from massive stars ionises their natal molecular cloud and creates an H II region. Photodissociation regions[1] (PDRs) are the transition from this H II region to the cold molecular cloud. While extreme-ultraviolet (EUV) radiation (>13.6 eV) dominates the photoionised layers, the stellar far-ultraviolet (FUV) radiation (6–13.6 eV) drives the physical and chemical processes in PDRs (Tielens & Hollenbach 1985a,b).

Most of the interaction between massive stars and their surroundings occurs in PDRs. While PDRs were initially associated with young massive stars (Tielens & Hollenbach 1985a), PDRs are also found in the diffuse ISM (Wolfire et al. 2003), reflection nebulae (e.g. Burton et al. 1990; Sheffer et al. 2011), planetary nebulae (Bernard-Salas & Tielens 2005), surfaces of proto-planetary disks (Vicente et al. 2013), pillars (McLeod et al. 2015), globules (Reiter et al. 2019), and molecular clouds. PDRs produce a significant fraction of the ISM radiative emission of galaxies, in particular in star-forming galaxies, (ultra-)luminous IR galaxies (ULIRGs), and galactic nuclei. The neutral ISM and most of the molecular ISM, where most of the ISM mass is found, does indeed reside in PDRs (Wolfire et al. 2022). Consequently, understanding PDRs is a key prerequisite for understanding star and planet formation and the large-scale ecology of the ISM of galaxies and its relationship to galaxy evolution.

The large-scale PDR structure is stratified with temperatures decreasing from 10^4 at the front surface of the PDR to a few hundreds of Kelvin in the atomic PDR, and, crossing the H_2 dissociation front, to a few tens of Kelvin deep into the molecular PDR. While models have been very successful in explaining the observed large-scale structure of PDRs (Tielens & Hollenbach 1985b; Sternberg & Dalgarno 1989; Abgrall et al. 1992; Le Bourlot et al. 1993; Röllig et al. 2007; Wolfire et al. 2022), recent high-angular resolution Atacama large millimeter/submillimeter array (ALMA) and Keck observations have revealed a varying PDR front and highly structured PDR (Goicoechea et al. 2016; Habart et al. 2023). The highly structured nature of the molecular PDR layers betrays the dynamic action of the evaporation flow that advects material from the molecular cloud, through the PDR and the ionisation front, into the ionised gas (Bertoldi & Draine 1996; Störzer & Hollenbach 1998; Henney et al. 2007). Hence, observations at a high angular resolution are required to resolve the small-scale structure to fully understand the processes responsible for shaping PDRs.

Observations at infrared (IR) wavelengths are key in understanding PDRs. Infrared spectra of PDRs are indeed extremely rich – they feature a plethora of strong H I recombination lines, fine-structure lines from atomic and ionised gas, rotational and ro-vibrational emission from H_2 and other small molecules, as well as broad emission bands commonly referred to as aromatic infrared bands (AIBs), all superimposed on undulating continuum emission. We note that some of this emission originates in the photoionised regions along the line of sight, rather than the PDR itself. This spectral diversity provides ample diagnostics to characterise the physical and chemical anatomy of PDRs and to characterise the photochemical evolution of molecules and dust (e.g. Marconi et al. 1998; Luhman et al. 1998; Walmsley et al. 2000; Sheffer et al. 2011; Pilleri et al. 2012; Habart et al. 2023). However, past IR observations had an insufficient angular resolution to resolve the small-scale structure of PDRs or were limited by the spectral resolution and/or wavelength coverage or both. The unprecedented capabilities of JWST allow, for the first time, for high spatial resolution (0.075″ to 0.173″) to be combined with medium spectral resolution and large IR wavelength coverage for PDR studies. Such observations thus provide the critical PDR diagnostics at an angular resolution that enables the highly structured PDR anatomy to be probed and the intricate combination of physical, chemical, and dynamical processes at play in shaping the PDR anatomy to be investigated.

[1] Also sometimes called 'photon-dominated regions' (e.g. Sternberg & Dalgarno 1995).

The PDRs4All Early Release Science (ERS) programme (ID1288)[2] fully exploits JWST's angular resolution by observing the nearest massive star-forming region, the Orion Nebula, in the NIRCam and MIRI imaging mode and NIRSpec and MIRI spectral mapping mode (Berné et al. 2022). This unique data set will serve as the reference data set for PDRs in the next decades and will facilitate the interpretation of numerous JWST observations. Indeed, given the prevalence of PDRs in the Universe and the strong IR emission of PDRs, much of the emission (to be) observed by JWST is from (unresolved) PDRs.

This work presents the first analysis of the PDRs4All NIRSpec data set and accompanies the PDRs4All NIRCam and MIRI imaging paper (Habart et al. 2024), the NIRSpec proplyd paper (Berné et al. 2024), the MIRI MRS PAH paper (Chown et al. 2024), and the MIRI MRS gas lines paper (Van De Putte et al. 2024). This paper is organised as follows. First, we describe the characteristics of the PDR, the Bar, as deduced from earlier studies in Sect. 2. This is followed by a description of the observations, data reduction and flux measurements in Sect. 3. A spectral inventory and line intensity list are given in Sect. 4.1 and Appendix B. Then, we discuss the spatial variation of gas and dust tracers and thus the PDR structure and anatomy in Sect. 5. We analyse the H I and He I recombination lines, the fluorescence lines, and the H_2, C I , and AIB emission to determine the physical conditions in the Bar in Sect. 6. Last, we discuss the Bar's structure in Sect. 7 and give a summary and conclusions in Sect. 8.

2. Bar

The Bar is a rim of the Orion molecular cloud core (OMC-1), the closest site of ongoing massive star-formation[3] (e.g. Genzel & Stutzki 1989; Bally 2008). The Bar is often referred as the 'Bright Bar' or 'Orion Bar' (e.g. Elliott & Meaburn 1974; Tielens et al. 1993; O'Dell et al. 2020). In the following, we name it the 'Bar'. The outskirts of OMC-1 are primarily illuminated by strong UV radiation from the O7V-type star θ^1 Ori C (Sota et al. 2011), the most massive star of the Trapezium cluster at the centre of the Orion Nebula and ∼2′ north-east of the Bar (e.g. Stacey et al. 1993; Luhman et al. 1994; O'Dell 2001; Goicoechea et al. 2015). Intense ionising radiation and strong winds from θ^1 Ori C (two main forms of stellar feedback in the region; Güdel et al. 2008; Pabst et al. 2019) power and shape the Orion Nebula, which is a blister H II region that is eating its way into the natal molecular cloud (located behind the cluster in our line of sight). The strong stellar UV radiation has carved out a large cavity in the background molecular cloud, where the inner concave regions tilt to form the Bar (e.g. O'Dell 2001).

The Bar historically refers to the elongated rim near the ionisation front (IF) that separates the edge of the molecular cloud from the surrounding H II region, with $n_e \simeq 5{\times}10^3$ cm^{-3} and $T_e \simeq 9{\times}10^3$ K at the IF (e.g. Weilbacher et al. 2015). The UV radiation impinging on the IF is (1–4)×10^4 times the mean interstellar field (e.g. Marconi et al. 1998). Some areas of the Bar may also be illuminated by the O5V-type star θ^2 Ori A, on the near side of the cluster (O'Dell et al. 2017). Beyond the IF, only far-UV (FUV) photons with energies below 13.6 eV pervade the Bar. This marks the beginning of the PDR. Because of its high temperatures and nearly edge-on orientation on the sky, the Bar shines at all wavelengths from optical to radio. Indeed, this PDR is the prototypical source to study the physical and chemical stratification caused by strong FUV radiation (e.g. Tielens et al. 1993; Hogerheijde et al. 1995; Jansen et al. 1995; van der Wiel et al. 2009).

The first layers of the Bar PDR are predominantly neutral and atomic, meaning $[H] > [H_2] \gg [H^+]$ (van der Werf et al. 2013; Henney 2021). The so-called 'atomic PDR' zone presents a plethora of IR atomic emission lines from low ionisation potential elements (recombination lines, forbidden lines, etc.; e.g. Walmsley et al. 2000). This warm (several hundred K) and moderately dense (n_H of a few 10^4 cm^{-3}) gas is mainly heated by photoelectrons ejected from Polycyclic Aromatic Hydrocarbons (PAHs), and mainly cooled by far-IR (FIR) [C II] 158 µm and [O I] 63 µm fine-structure lines (e.g. Tielens et al. 1993; Herrmann et al. 1997; Bernard-Salas et al. 2012; Ossenkopf et al. 2013). In addition, this extended atomic PDR zone coincides with the peak of very bright AIB emission (e.g. Bregman et al. 1989; Sellgren et al. 1990; Tielens et al. 1993; Giard et al. 1994; Knight et al. 2021).

At about 15″ (∼0.03 pc) from the IF, the flux of FUV photons is sufficiently attenuated that most of the hydrogen becomes molecular. This position marks the critical H/H_2 transition zone, the dissociation front (DF). The DF displays several IR rotational H_2 and the HI 21 cm emission lines (e.g. Parmar et al. 1991; van der Werf et al. 1996, 2013; Allers et al. 2005; Shaw et al. 2009). In addition, H_2 lines from FUV-pumped vibrationally excited levels up to $v = 14$ are detected (Luhman et al. 1994; Kaplan et al. 2017, 2021). Reactive molecular ions such as CH^+, SH^+, CO^+ or OH^+ start to form close to the DF (e.g. Stoerzer et al. 1995; Fuente et al. 2003; Nagy et al. 2013; van der Tak et al. 2013; Goicoechea et al. 2017). The first steps of PDR chemistry are triggered by the presence of vibrationally excited H_2, whose internal energy overcomes the endoergicities and energy barriers of key gas-phase reactions (e.g. Goicoechea & Roncero 2022) and, thus, initiates the formation of molecular hydrides (e.g. Tielens & Hollenbach 1985a; Sternberg & Dalgarno 1995; Agúndez et al. 2010).

The transition from C^+ to C to CO is expected to take place beyond the DF, where the PDR becomes mostly molecular. That is, $[H_2] \gg [H]$. However, observations have not accurately settled the exact position of the C^+/C/CO transition zone (e.g. Tauber et al. 1995; Wyrowski et al. 1997; Cuadrado et al. 2019; Salas et al. 2019). The CO gas temperature just beyond the DF is $T_k \simeq 200$–300 K (Habart et al. 2010; Joblin et al. 2018) and decreases further into the molecular cloud. This confirms the presence of a sharp (gas and dust) temperature gradient from the H II region interface to the molecular cloud interior (Arab et al. 2012; Salgado et al. 2016). Despite the strong irradiation conditions, the so-called 'molecular PDR' ($n_H \simeq 10^5$-10^6 cm^{-3}) shows a rich chemical composition, including a large variety of small hydrocarbons and complex organic species (e.g. Hogerheijde et al. 1995; Simon et al. 1997; Peeters et al. 2004; Leurini et al. 2006; Cuadrado et al. 2015, 2017). Dense clumps ($n_H \simeq 10^7$ cm^{-3}) with angular sizes of ∼5″ (∼2000 au) are known to exist deeper inside the Bar (e.g. Tauber et al. 1994; van der Werf et al. 1996; Young Owl et al. 2000; Lis & Schilke 2003). However, it is not clear whether these clumps will ultimately form stars and whether smaller (sub-arcsecond) clumps can exist closer to the DF (e.g. Gorti & Hollenbach 2002;

[2] https://pdrs4all.org

[3] The most commonly adopted distance to the Bar is 414 pc (Menten et al. 2007) although recent GAIA observations suggest slightly lower values (Kounkel et al. 2018; Großschedl et al. 2018). We refer to Habart et al. (2024) for a discussion. In this paper we adopt a distance of 414 pc. Hence, 1″ roughly corresponds to 0.002 pc.

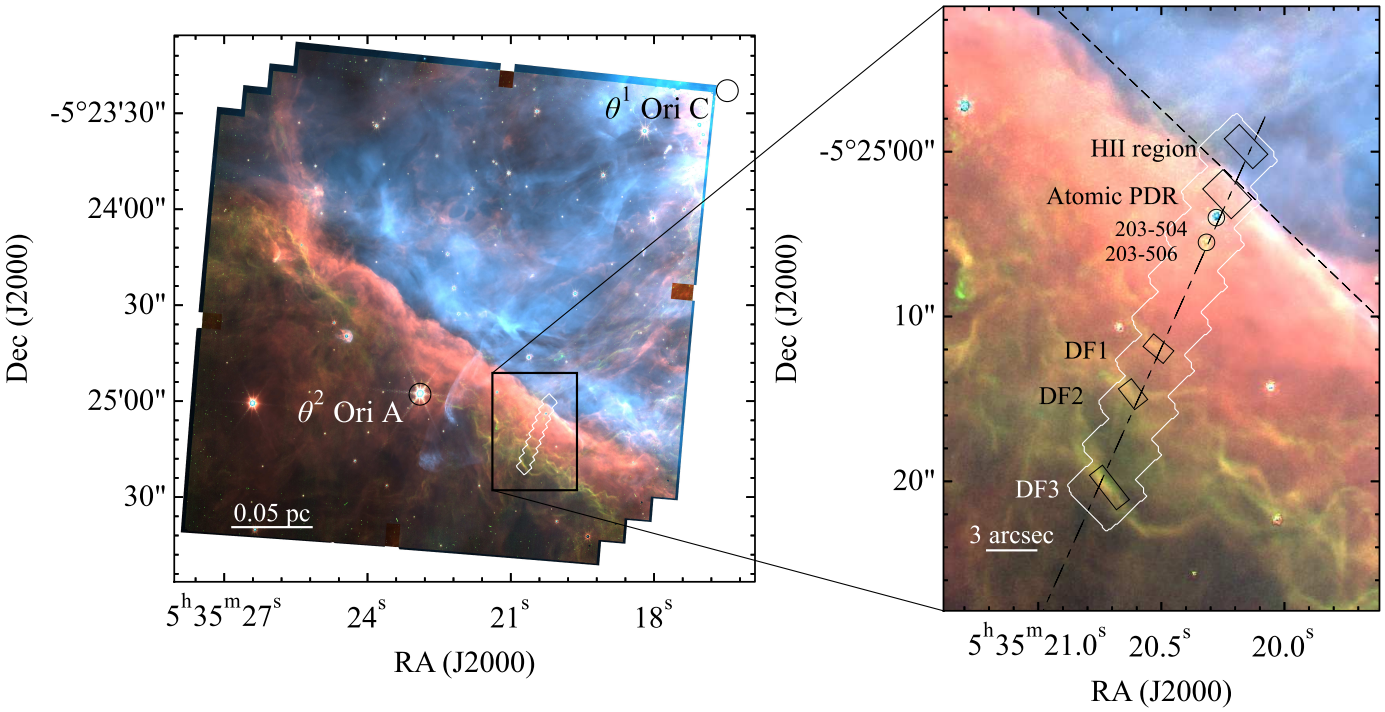

Fig. 1. Composite NIRCam image of the Bar showing the NIRSpec mosaic footprint (white boundary). The composite image is composed of F335M (AIB emission) in red, F470N-F480M (H_2 emission) in green, and F187N (Paschen α emission) in blue (Habart et al. 2024). Bright stars θ^1 Ori C and θ^2 Ori A are indicated with black circles in the left panel. In the right panel the five black boxes indicate the apertures used to extract our five template spectra. The dot-dashed line indicates the cut perpendicular to the Bar (position angle, PA, of 155.79°), while the dashed line indicates the position of the ionisation front in the NIRSpec FOV (PA=46.21°). The protoplanetary disks 203–504 and 203–506 are indicated with black circles.

Andree-Labsch et al. 2017). If they exist, additional heating by collisional de-excitation of vibrationally excited H_2 will keep their irradiated surfaces very hot, at several thousands K (e.g. Burton et al. 1990).

Unfortunately, most of our knowledge of the Bar comes from modest angular resolution observations (~5″–40″), especially at FIR to radio wavelengths, that do not spatially resolve the main transition zones of the PDR. Consequently, their fundamental structures: homogeneous versus clumpy, physical conditions, chemical composition, and role of dynamical effects are not fully known. ALMA provided the first ~1″ resolution images of the CO and HCO^+ emission (Goicoechea et al. 2016). Instead of an homogeneous PDR with well-defined and spatially separated H/H_2 and C^+/C/CO transition zones, ALMA revealed rich small-scale structures (akin to filaments and globulettes), sharp-edges, and uncovered the molecular emission from a protoplanetary disk (203–506; Bally et al. 2000; Champion et al. 2017). Even spatially sharper IR photometric images with the Keck telescope (using adaptative optics) uncovered the presence of not a single, but several small-scale photodissociation fronts (Habart et al. 2023). Our JWST/NIRSpec integral field observations across the Bar, from the H II region to the main molecular dissociation fronts (and including the protoplanetary disks 203–504 and 203–506), represent the first sub-arcsecond spectroscopic study of this prototypical PDR. This study complements our first JWST photometric images of the Bar (Habart et al. 2024), which show an unprecedented view of the region, revealing very complex small-scale PDR structures, and ridges, and a 3D terraced distribution of multiple dissociation fronts that contrasts with the classical 1D view of the H/H_2 and C^+/C/CO transition zones of a PDR.

3. Observations, data reduction, and analysis

3.1. Observations

The observations are part of the Early Release Science programme PDRs4All: Radiative feedback from massive stars (ID: 1288, PIs: Berné, Habart, Peeters; Berné et al. 2022)[4]. We obtained our observations using the NIRSpec instrument (Jakobsen et al. 2022) onboard the JWST (Gardner et al. 2006) in the integral field unit (IFU) mode (Böker et al. 2022), which provides spatially resolved imaging spectroscopy. This resulted in a 9 × 1 mosaic covering 3″ × 25″ and centred on position α(J2000) = 05 35 20.4749, δ(J2000) = –05 25 10.45 with a position angle (PA) of 43.74° in the 0.97–5.27 μm range at a angular resolution of 0.075″ to 0.173″ and with a pixel size of 0.1″×0.1″. The field of view (FOV) of the NIRSpec mosaic is shown in Fig. 1. We also obtained background observations using a single pointing centred on position α(J2000) = 05 27 19.400, δ(J2000) = –05 32 04.40. For our science and background observations, we used the three high spectral resolution, R~2700, gratings (G140H, G235H, and G395H) covering the wavelength range from 0.97 to 5.27 μm, the NRSRAPID readout mode (as this mode is appropriate for bright sources), and a 4-point dither pattern. To quantify the leakage of the Micro-Shutter Array (MSA), we used the most accurate strategy for taking imprint exposures to date, that is we obtained imprint exposures with the same exposure time as the science (and background) exposures at all dither positions. Five groups per integration with one integration per exposure are used, for a total on-source integration time of 257.7 s.

[4] DOI: 10.17909/pg4c-1737.

3.2. Data reduction

We download the uncalibrated Level 1 science and background NIRSpec IFU data from the MAST portal. We reduce the data using the JWST Science Calibration Pipeline (version 1.10.2.dev26+g8f690fdc) and context jwst_1084.pmap of the Calibration References Data System (CRDS). First, we perform detector-level corrections on science, background, and imprint exposures in the Detector 1 step. Then we correct the resulting rate files for $1/f$ noise correction using the algorithm provided by the helpdesk. The algorithm measures the pattern in the unilluminated pixels in a given rate file using a column-by-column rolling median basis and subtracts it from the data in the illuminated pixels of that file. These cleaned rate files are then used as input for calibrations of individual exposures in the Spec 2 step. Finally, we combine all exposures to build cubes in Spec 3. We note that we disabled the outlier detection step in Spec 3 because it introduces artefacts and removed bright lines from our data. Lastly, we point out that we reduce the data of each pointing in a given spectral segment separately, yielding 27 spectral cubes from 9 pointings in three spectral segments at the end of the Spec 3 step of the pipeline.

While the pipeline is able to produce a mosaic that combines all pointings over the full wavelength range, this results in some undesirable artefacts such as stripes near pointing edges. By building the mosaic outside of the pipeline, we can apply calibration factors to single-segment cubes (to improve the overall flux calibration), and we can specify precisely how we want to deal with overlapping data (spatially and spectrally).

Starting with spectral cubes generated by the JWST pipeline, we create the final mosaic using the following approach.

1. We use the Astropy-affiliated package for image reprojection `reproject`, and the `reproject.find_optimal_celestial_wcs` routine on all of the 27 input cubes (9 pointings, 3 segments each) to determine the World Coordinate System (WCS) information and array shape of the final cube.
2. Next, we use `reproject.reproject_exact` to reproject every wavelength-plane of these 27 cubes to the final cube shape and WCS.
3. A physical gap between NIRSpec's detectors leads to a gap of missing wavelengths in each IFU cube (for details see Böker et al. 2022). The wavelength gap spans bluer wavelengths in the northern part of each pointing and smoothly shifts to redder wavelengths towards the southern part of each pointing. As best as possible, we use data from adjacent pointings to fill in these gaps. For spaxels that are covered by two partially overlapping pointings, we coadd the overlapping spectra unless one of the spaxels is either missing flux, or is within a 9-pixel distance from the respective pointing edge (a 9 pixel distance was chosen to avoid edge effects). If a spaxel fills in flux that is missing from an overlapping spaxel due to a wavelength gap, we use `specutils.manipulation.FluxConservingResampler` to resample the fluxes onto the wavelength grid of the cube where flux is missing. We resample onto the wavelength grid of the pointing with missing flux because the number of spaxels that require interpolation is a small minority of the total number of spaxels, and because all spaxels in the mosaic need to be on the same wavelength grid – only spaxels from the cube that are affected by the wavelength gap need to be dealt with separately. As a consequence, not all pixels in the extraction aperture contribute at a given wavelength in the wavelength gap region. For cases where one of the two spatially overlapping spaxels is within 9 pixels of the edge of its respective pointing while that of the other pointing is not, the spaxel that is closer to the edge of its pointing is ignored – at that location, the mosaic contains the spaxel that is further from its pointing edge.
4. We then ensure that the NIRSpec flux calibration is accurate by computing synthetic NIRCam images from the NIRSpec cubes, then reproject background-subtracted NIRCam images onto the NIRSpec pixel grid, and then compare the synthetic NIRCam flux against the true NIRCam flux in each pixel. Similar to the cross-calibration method between imaging and IFU observations of Kraemer et al. (2022) using *Spitzer*/IRAC and *Spitzer*/IRS data, we perform a linear regression on the pixel-by-pixel synthetic NIRCam flux vs. true NIRCam flux. The best-fit slope of this relationship (for each NIRCam filter) is our estimate of the cross-calibration factor between NIRCam and NIRSpec. The best-fit parameters are tabulated in Table A.1 (see Chown et al., in prep., for details).
5. We then multiply the G235H and G395H NIRSpec mosaics and their uncertainties by their respective calibration factors. Since we do not have background-subtracted NIRCam data in any filters that overlap with the G140H wavelength range, we are unable to assess the flux calibration of that segment in the same way. We multiply the G140H mosaic by the calibration factor for the G235H segment. We tested an approach where each G140H spaxel was scaled to match the flux in the overlapping G235H spaxel, but we found this approach to be unreliable due to the presence of data reduction-related artefacts.

The applied reduction process produces very high quality data. However, after processing the raw data, some artefacts remain in the data. The remaining artefacts that are present include:

1. Bright circular artefacts that are localised in wavelength (a few spectral bins) and in position (roughly circular, a few pixels wide, and in the same positions on the detector).
2. Vertical stripes at the edge of each pointing (N-NW to S-SE direction) with lower flux, likely due to the fact that a path loss correction using flight data cannot be performed using the available reference files.
3. A sinusoidal wave pattern in the uncertainty data of the three segments.
4. Fluxes within a few wavelength bins of a gap are generally unreliable.
5. A roughly sinusoidal wave pattern in the surface brightness and/or broad absorption/emission features in gratings G140H and G235H in the NRS2 detector[5]. As these are not present in the grating covering the subsequent wavelength range in the NRS1 detector, this is likely residual $1/f$ noise (the effects of $1/f$ noise are more pronounced on the NRS2 detector compared to the NRS1 detector).

We mask out the bright circular artefacts, and replace bad data from vertical stripes with better data when co-adding adjacent pointings as mentioned above[6].

We extract spectra in five apertures (Fig. 1 and Table A.2) by applying a 3-σ cut to remove bad data and calculating the inverse-variance weighted average of spaxels within each aperture. We use five large extraction apertures positioned in front of the ionisation front (IF), at the peak of the PAH emission, and at the three H/H_2 dissociation fronts (DF 1, DF 2, DF 3) in the

[5] The NRS1 (NRS2) detector covers wavelengths below (beyond) the wavelength gap in each segment.
[6] See acknowledgments for data availability.

mosaic. The resulting spectra thus serve as templates for the H II region, the atomic PDR and the molecular PDR. In addition, to measure quantities from weaker lines as a function of distance from θ^1 Ori C, we spatially rebin the spectral mosaic to a 2×2 spaxels scale prior to fitting the lines.

3.3. Flux measurements

We measure the flux of selected emission lines by fitting a Gaussian line profile of a fixed full width at half maximum (FWHM) set by the spectral resolution at that wavelength. We determine the spectral resolution by using the resolution curves for the G140H, G235H, and G395H gratings given in the Jdox[7]. Before performing a fit, we subtract a linear continuum. We visually select a wavelength range for continuum determination that is devoid of emission lines. Given the presence of artefacts in the data set and the fact that the wavelength range for fitting is very small, we find that subtracting an offset for the continuum instead of a linear continuum works better when measuring fluxes across the entire spectral map. Lines located on top of the strong 3.3 μm AIB are fit after removal of the AIB emission (see Sect. 6.6.1 for details). Given the large number of lines present in the template spectra (~600), we model the continuum using a non-linear iterative peak-clipping algorithm[8] to provide the fluxes for the entire line inventory (see Appendix B). In the 3–3.7 μm region, we use the fit to the AIB emission instead as the continuum.

For the uncertainties on the measured fluxes, we use the flux uncertainties from the Gaussian fit of the line which takes into account the uncertainties on the surface brightness provided by the data reduction pipeline. We note that the uncertainties resulting from the pipeline are too low and therefore, the quoted flux uncertainties likely underestimate the true uncertainties. In addition, uncertainties in the continuum determination are not included[9]. To assess the influence of the artefacts on the line fluxes, we compare selected line fluxes with their corresponding NIRCam filter combination (see Habart et al. 2024, their Fig. 11) and conclude that the agreement with NIRCam is excellent. Indeed, despite remaining systematic artefacts in the data set, the change in intensities of Br α, Pa α, [Fe II] at 2.1644 μm, H_2 0–0 S(9), H_2 1–0 S(1), and total AIB emission across the PDR matches their spatial behaviour as observed by NIRCam very well. In addition, the Br α, Pa α, H_2 0–0 S(9), and total AIB emission agree within 3% on the absolute scale with their corresponding (continuum subtracted) NIRCam filter (note the AIB filter does not require continuum subtraction). Deviations are larger for the [Fe II] at 2.1644 μm, and H_2 1–0 S(1) emission as these transitions do not dominate the emission captured by the corresponding (continuum subtracted) NIRCam filter[10].

4. Spectral inventory

4.1. Template spectra of the Bar

The five template spectra probing the H II region, the atomic PDR, and the molecular PDR (see Sect. 3.2) are shown in Fig. 2 and in more detail with line labels in Fig. B.1. These 0.97–5.27 μm near-IR (NIR) spectra reveal a spectacular richness of spectral lines and bands on top of weak continuum emission (see Table B.1 for full inventory and line intensities). In particular at the shortest wavelengths, numerous (blended) emission lines are present to the point of the line confusion limit.

Across the mosaic, H I recombination lines are detected from the Paschen series (up to principal quantum number $n_u = 7$ in all template spectra) and the Bracket, Pfund, Humphreys, and $n_l = 7$ series (up to $n_u = 25$–40 in the molecular PDR; $n_u = 45$–50 in the H II region and atomic PDR). We also detect numerous He I recombination lines as well as emission lines from Fe II and Fe III, C I recombination lines, O I and N I fluorescent emission, the Si II, P II, and K III emission line(s), and the [Kr III] 2.1986 μm transition. In addition to atomic and ionic lines, the NIR spectra of the Bar show many high-energy ro-vibrational lines from simple molecules (H_2, HD, CO, and CH^+). These lines are generally faint and become apparent deeper inside the molecular layers of the PDR (DF 1, DF 2, and DF 3 templates), where most of the hydrogen is locked up in H_2.

The molecular emission is dominated by a forest of H_2 lines from vibrationally excited bands ($v = 1$–0, $v = 2$–1, etc.), with detections up to $v = 6$. Kaplan et al. (2021) previously reported on the detection of some of these lines (in the 1.45–2.45 μm range) from ground-based observations at higher spectral resolution than NIRSpec (R~45 000), but at significantly lower angular resolution (0.3″ pixel scale). These vibrationally excited levels are populated by far-UV (FUV) pumping in the Lyman and Werner bands of H_2, followed by radiative and collisional de-excitation (Black & Dalgarno 1976; Sternberg & Dalgarno 1989; Burton et al. 1990). Interestingly, we also detect ro-vibrational lines of the HD isotopologue in the $v = 1$–0 band at ~2.6 μm (the R branch, Figs. 3, B.1).

In addition, we detect high-J H_2 pure rotational lines in the ground vibrational state, up to $v = 0$–0 $S(19)$, involving very high-energy rotational levels; $E_u/k \simeq 30{,}000$ K. Moreover, we report on the first detection of H_2 pure rotational lines within the vibrationally excited states $v = 1$ (up to $v = 1$–1 $S(17)$) and $v = 2$ ($v = 2$–2 $S(13)$). These highly excited rotational levels are populated by the radiative and collisional de-excitation of FUV-pumped levels.

Quite unexpectedly we report on the first detection, towards an interstellar PDR, of the CO $v = 1$–0 and $v = 2$–1 bands centred at 4.7 μm (Fig. 3). Detected ro-vibrational lines are faint but seen up to high J values. This implies that rotational levels within the vibrational state $v = 2$, with energies of about $E/k \simeq 7000$ K, are populated in the PDR. These are substantially higher energies than those of the highest-J pure rotational line ($v = 0$–0, $J = 23$–22) detected in the far-IR ($E_u/k \simeq 1500$ K; Joblin et al. 2018).

Concerning other hydride molecules previously detected in the Bar through rotational spectroscopy of the $v = 0$ state (e.g. Gerin et al. 2016), we detect CH^+ $v = 1$–0 ro-vibrational lines at ~3 μm (see spectroscopic analysis in Changala et al. 2021). Far-IR pure rotational lines of CH^+ up to $v = 0$–0, $J = 5$–6 were first detected by Nagy et al. (2013) at the much lower (~10″) angular resolution with the Herschel space telescope. Here we detect CH^+ $v = 1$–0 ro-vibrational lines towards both the atomic PDR and the molecular PDR (DF 1, DF 2, and DF 3; Fig. 4). This likely indicates that small molecular fractions of H/H_2 are enough to form sufficient CH^+ and to excite the $v = 1$–0 band through chemical formation pumping (CH^+ is a very reactive molecular ion; e.g. Nagy et al. 2013; Godard & Cernicharo 2013). The NIR CH^+ $v = 1$–0 band has stronger P-branch

[7] https://jwst-docs.stsci.edu/jwst-near-infrared-spectrograph/nirspec-instrumentation/nirspec-dispersers-and-filters

[8] Statistics-sensitive Non-linear Iterative Peak-clipping algorithm from pybaseline https://pybaselines.readthedocs.io/en/latest/

[9] In case of continuum determination using a non-linear iterative peak-clipping algorithm, the uncertainties are asymmetric with the upper bound being larger than the lower bound.

[10] See acknowledgements for data availabillity of all maps and profiles along the NIRSpec cut.

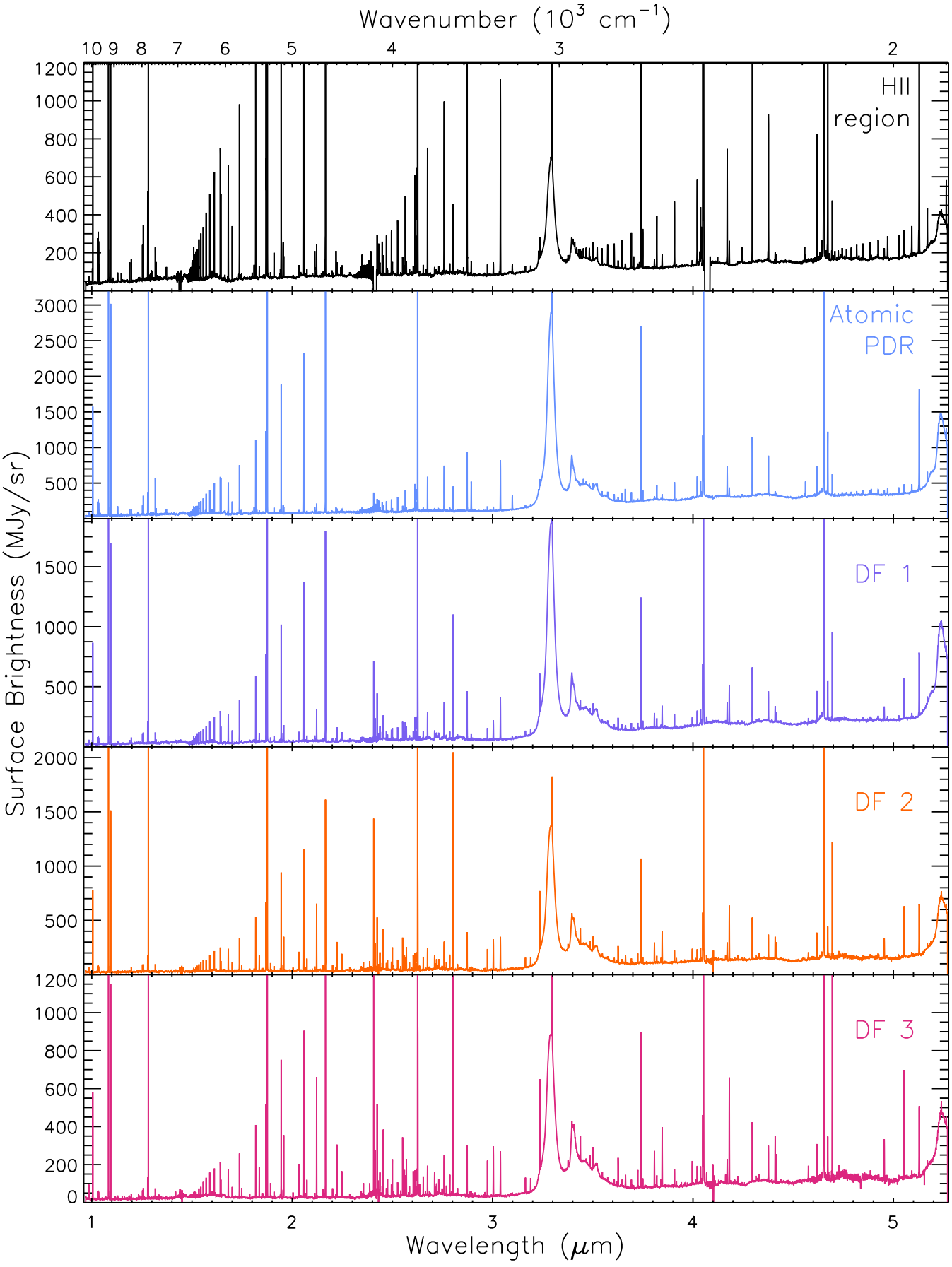

Fig. 2. Template spectra representing, from top to bottom, the H II region, the atomic PDR, and the dissociation fronts DF 1, DF 2, and DF 3.

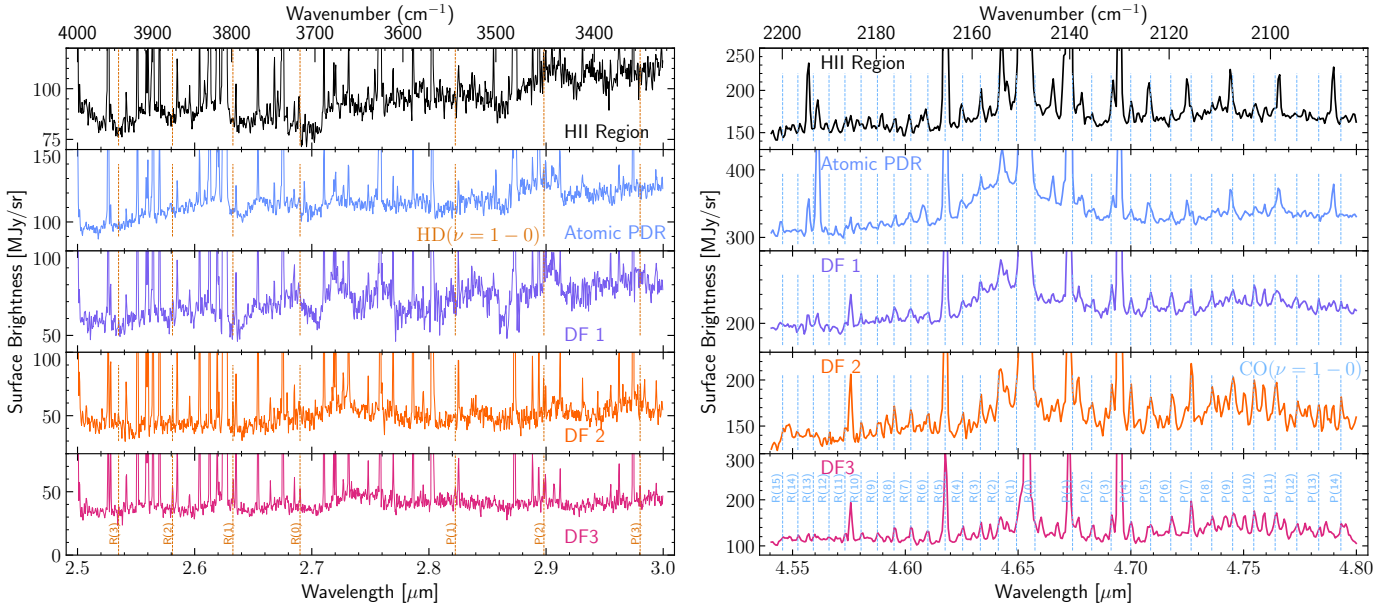

Fig. 3. Detection of the HD v = 1–0 ro-vibrational lines at ~2.6 μm (left) and of the CO v = 1–0 band centred at 4.7 μm in the molecular PDR (right). For the CO v = 2–1 band detection, see Fig. B.1.

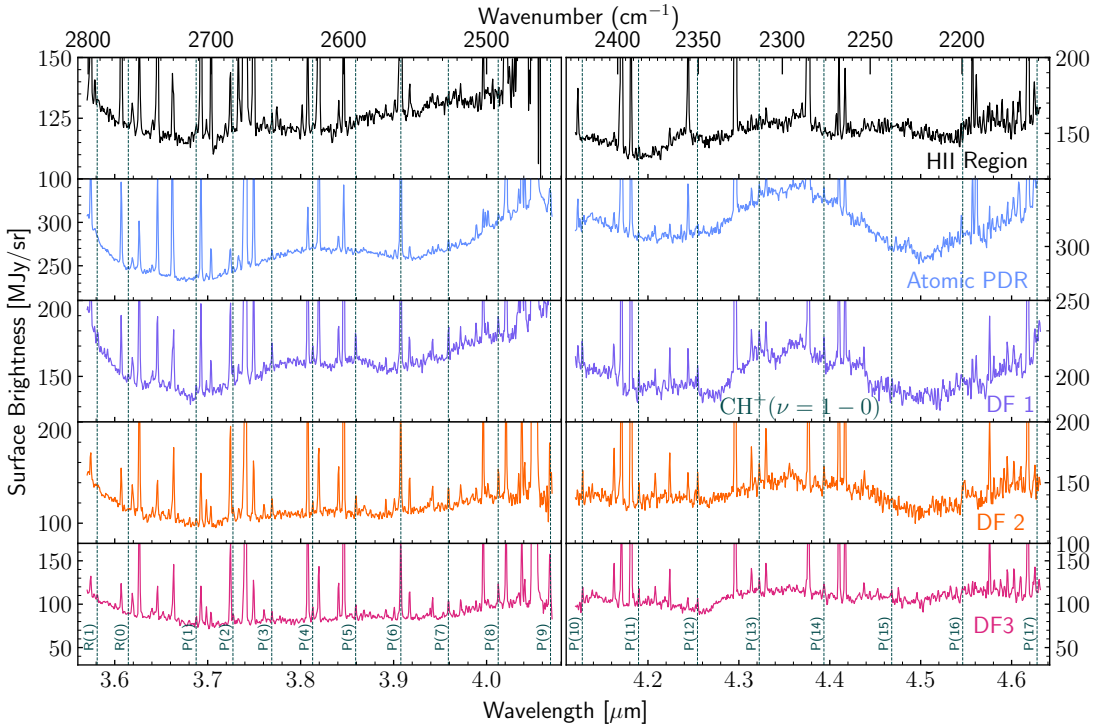

Fig. 4. Detection of the CH^+ v = 1–0 ro-vibrational lines in the atomic PDR, DF 1, DF 2, and DF 3.

lines than *R*-branch lines (nearly undetected), a spectroscopic behaviour previously reported and explained by Neufeld et al. (2021) towards the planetary nebula NGC 7027. For a detailed analysis of the CH^+ v = 1–0, we refer the reader to Zannese et al. (in prep.).

We observe weak continuum emission with increasing surface brightness towards longer wavelengths. The continuum emission does not increase in surface brightness towards the shortest wavelengths, indicating there is not a strong contribution from scattered light from young massive stars such as θ^1 Ori C. The Orion Nebula hosts many low and intermediate mass stars (Hillenbrand & Carpenter 2000) which can contribute to the observed continuum emission (by scattering). In addition, the observations are consistent with a continuum contribution from stochastically heated very small grains and/or blended overtone and combination bands from PAHs (see Sect. 5.1). A detailed breakdown of the various continuum contributors will be investigated in a forthcoming paper (Onaka et al. in prep.).

The observations also display strong aromatic infrared bands (AIBs; Fig. 5). The strong 3.29 μm AIB along with weaker bands at 3.25, 3.40, 3.46, 3.52, 3.56 μm are perched on top of a broad plateau (see also Geballe et al. 1989; Sloan et al. 1997). We report

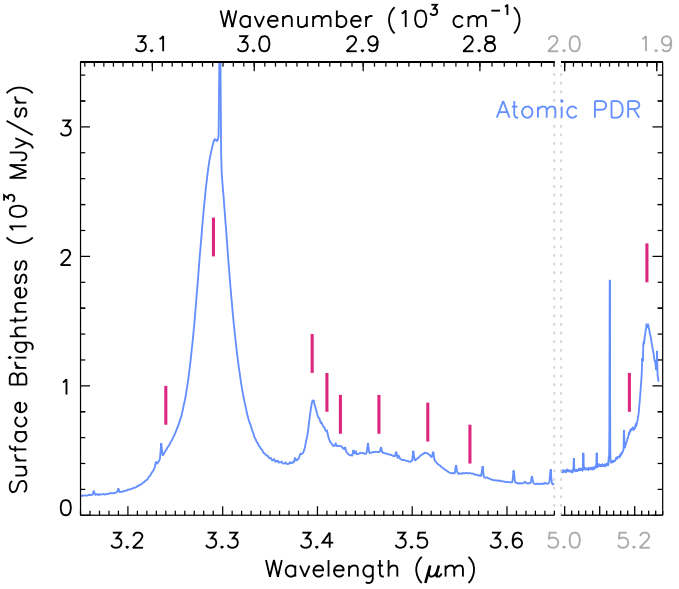

Fig. 5. Components of the AIB emission detected in the atomic PDR.

that the 3.40 μm band is composed of three sub-components centred at 3.395, 3.403, and 3.424 μm. An additional AIB band is (partially) detected at 5.236 μm. This band has a blue shoulder peaking near 5.18 μm. While the bands at ∼3.4 μm are aliphatic in nature (see Sect. 6.6), we refer to these bands as the AIBs in the remainder of the paper.

While the detection of weak broad features is very challenging given the current calibration (Sect. 3.2), Fig. 6 reveals broad structures in the 3.5–5.2 μm range[11]. All templates, except the H II region template, show enhanced emission (with respect to a linear continuum) from ∼3.1 μm to ∼4.9 μm. We rule out an artificial decrease in flux near 4.5 μm, which is much less pronounced in the H II region template, because the template spectra match the MIRI-MRS continuum (starting at 4.9 μm) very well indicating the flux levels near 5 μm are accurate. Consequently, the templates tentatively show a lack of emission or an absorption feature near 4.5 μm. We are unaware of any known absorption feature near 4.5 μm of similar width and thus favour the interpretation of a lack in emission. If born out, such an extended emission (band) has not been seen before, likely due to the lower angular resolution and incomplete wavelength coverage, and, in some cases, low data quality, and may arise from blended overtone and combination bands from PAHs (Allamandola et al. 1989). A detailed investigation of its characteristics will be presented in a forthcoming paper. The templates show an asymmetric band (with a red wing) centred at 4.644 μm and potentially an asymmetric band (with a red wing) centred at 4.746 μm (see also Appendix H.2). The CD stretching mode in deuterated PAHs, occurs between 4.54 and 4.75 μm (Hudgins et al. 2004; Buragohain et al. 2015; Yang et al. 2020, 2021; Allamandola et al. 2021). In particular, the CD stretch in PAHs to which D atoms are added (DPAHs) occurs near 4.6 μm (2170 cm^{-1}), whereas the CD stretch in deuterated methyl groups near 4.7 μm (2130 cm^{-1}). This band has been observed in Orion and a few other H II regions (Peeters et al. 2004; Onaka et al. 2014, 2022; Doney et al. 2016), although the band profile could not be resolved due to the low angular and spectral resolution. The atomic PDR and, perhaps, DF 1 also show two broad emission bands centred near 3.8 μm (with a width of ∼0.5 μm) and near 4.35 μm. These bands coincide with a nitrile (-CN) stretch at 4.38 μm (2280 cm^{-1}) and at 4.52 μm (2220 cm^{-1}), and the CD stretch for PAHs in which a peripheral H atom is replaced by a D atom (PADs), near 4.4 μm (4.3–4.5 μm range; Hudgins et al. 2004; Allamandola et al. 2021)[12]. Lastly, DF 3 shows a potential band in absorption near 4.27 μm that could arise from the C=O antisymmetric stretching mode in CO_2 ice. However, the presence of CO_2 ice in the PDR is unlikely given the physical conditions in the dissociation front (e.g. hot gas temperature, warm grains, low A_V) and the apparent lack of H_2O ice. Improved data reduction and/or further observations may have to confirm the reality of this feature.

4.2. Reference line list

To facilitate the identification of detected lines in the present observations as well as in future JWST observations, we prepared a line list based on model calculations using the Cloudy (Ferland et al. 2017) and Meudon PDR codes (Le Petit et al. 2006). A detailed description of these model calculations can be found in Berné et al. (2022). These model calculations include lines with intensities greater than 5×10^{-10} W m^{-2} sr^{-1}. After the data arrived, we expanded the line list to include all detected lines. The resulting line list includes hydrogen recombination lines with the upper principal quantum number up to 50 and all the lines of molecular hydrogen listed in Roueff et al. (2019). We also include [Fe III], [Ni II], and [Ni III] lines, which were not included in the Cloudy simulation but are detected in the ionised region (see also Van De Putte et al. 2024). O I and N I fluorescence lines are added with the criteria that the Einstein-A coefficients are larger than 5×10^5 s^{-1} and 0.9×10^5 s^{-1} for N I and O I, respectively. The criteria are chosen to include all detected lines. For molecular lines, we include the rovibrational lines of HD up to $v = 3$ and those of CO with $v = 1$–0 and 2–1. Some of these transitions are also detected in the molecular PDR. In addition, the lines of CH^+ and OH are included; the latter is detected in the proplyd 203–506, which is located within the NIRSpec mosaic (Berné et al. 2023; Zannese et al. 2023). Finally, the list also contains several dust bands, including strong absorption bands of ice species, major AIBs, and C_{60}.

The line list contains the transition wavelength in vacuum, assignment of the transition, upper level energy, and Einstein A-coefficient. Atomic transition data are taken from the atomic line database at University of Kentucky (van Hoof 2018)[13]. For molecular hydrogen, we refer to Roueff et al. (2019). We adopt the CO and HD data from the HITRAN (Gordon et al. 2022)[14]. We used the data of Changala et al. (2021) for CH^+ and the OH data collected by Tabone et al. (2021) and Zannese et al. (2024) using Yousefi et al. (2018) and Brooke et al. (2016). Values in Brieva et al. (2016) are used for C_{60}, while the data in Sect. 6.6 (Gaussian decomposition) and Chown et al. (2024) are taken for the AIBs shortwards of 17 μm while the data from Smith et al. (2007) are taken for the AIBs longwards of 17 μm. For the ice species, we refer to Gibb et al. (2004) and Boogert et al. (2015).

The present line list contains nearly 7000 lines and dust bands, which are potentially detectable by NIRSpec and

[11] We note that the NRS1 detector covers wavelengths up to 3.983–4.099 μm, whereas the less reliable NRS2 detector covers wavelengths larger than 4.086–4.203 μm depending on the IFU virtual slit. However, no artefacts are known at the positions of these structures (per the JWST helpdesk).

[12] We note that this also coincides with an aldehyde (-CHO) stretch at 3.8 μm (2600 cm^{-1}), however, this would also give a C=O stretch near 5.9 μm that is not detected (Champion et al. 2017).

[13] https://www.pa.uky.edu/~peter/newpage/

[14] https://hitran.org

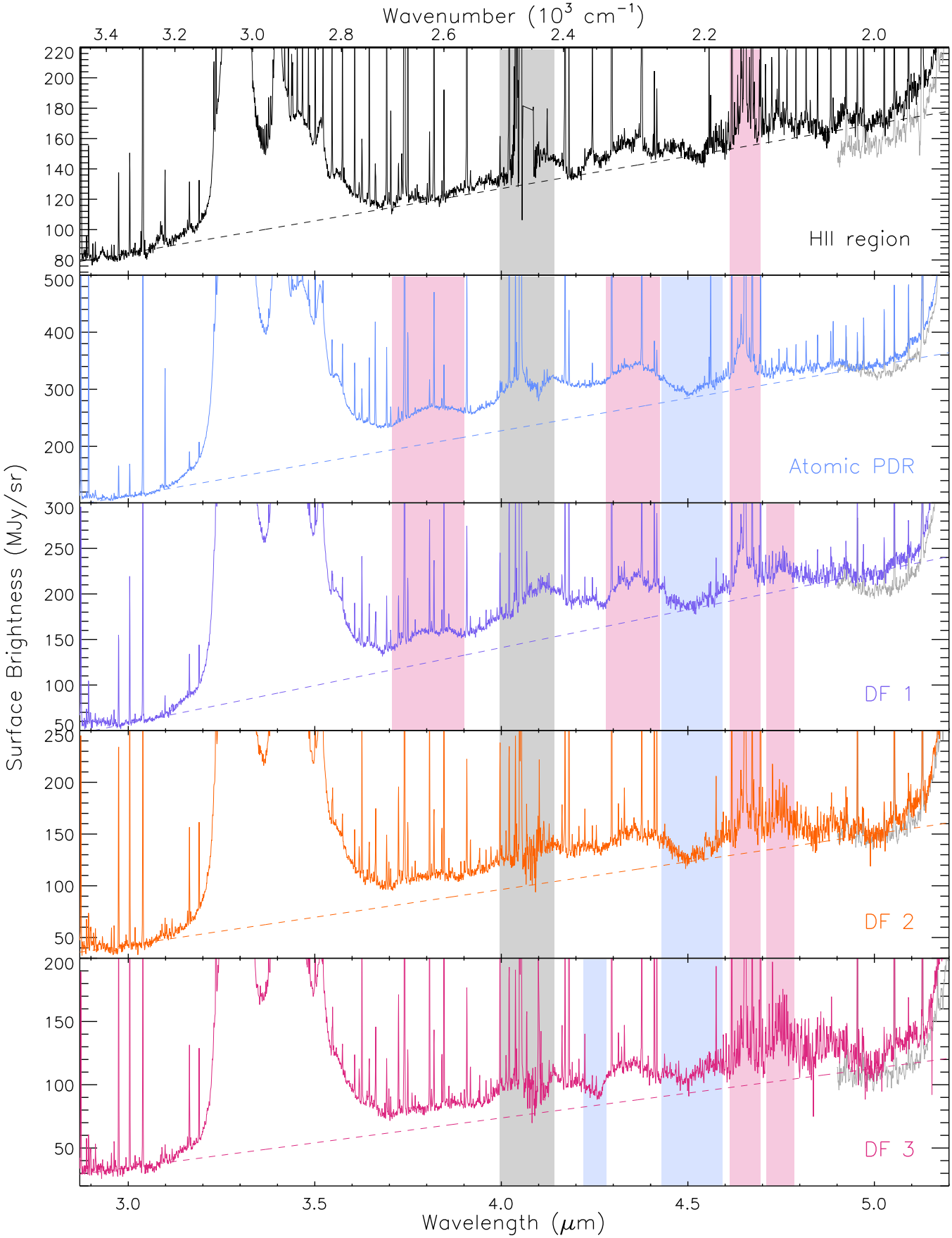

Fig. 6. Illustration of excess broadband emission between 3 and 5 μm. Close to the wavelength gap, fluxes are often unreliable (Sect. 3.2; indicated by the grey shaded area). The MIRI spectra are shown in light grey. The dashed lines show a linear continuum matched with the data near 2.98 and 4.99 μm. Red (blue) shaded boxes indicate tentative emission (absorption) bands. See Sect. 4.1 for a discussion.

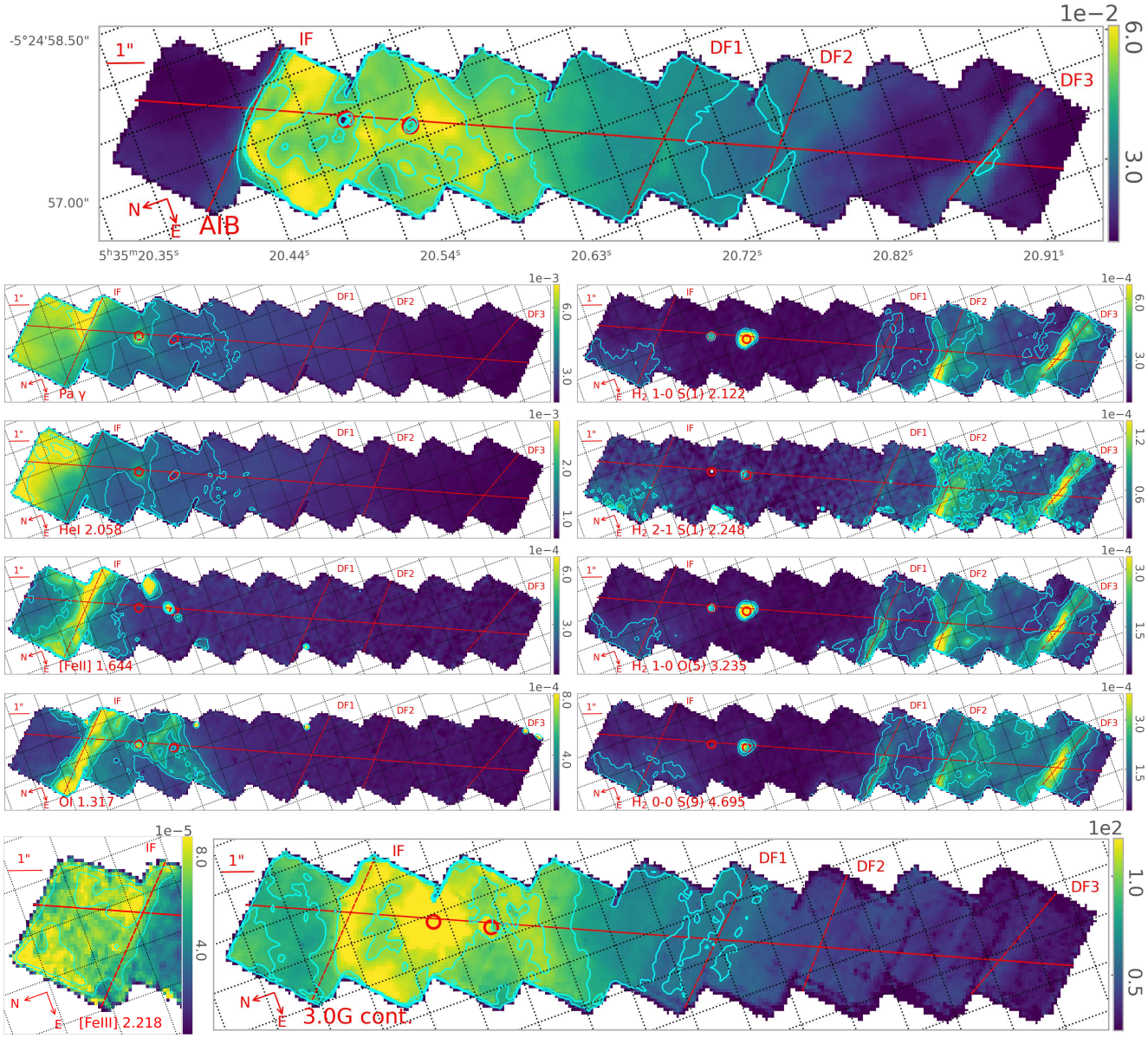

Fig. 7. Bar as seen in selected transitions in units of erg cm^{-2} s^{-1} sr^{-1}. No extinction correction is applied. Starting at the top, we show an image of the total AIB emission (i.e. sum of all AIB components in the 3.2–3.7 μm range). Following that, (from top to bottom) we show Pa γ, He I 2.058 μm, [Fe II] 1.644 μm, O I 1.317 μm, and [Fe III] 2.218 μm in the left column and H_2 1–0 S(1), H_2 2–1 S(1), H_2 1–0 O(5), H_2 0–0 S(9), and the continuum from the Gaussian decomposition at 3 μm (MJy sr^{-1}) in the right column. We set the colour range from the bottom 0.5% to the top 99.5% intensity levels of the data for each map (across the entire NIRSpec mosaic), excluding values of zero, edge pixels, and the two proplyds (as well as the surrounding region of the proplyds for the continuum). White pixels inside the mosaic indicate values of zero reflecting issues with the data. The nearly horizontal red line indicates the NIRSpec cut and the nearly vertical red lines indicate from left to right the IF and the DFs (DF 1, DF 2, DF 3). The two proplyds are indicated by the circles. Across the entire NIRSpec mosaic, contours show the 52, 75, and 90% intensity levels of the data for AIB, 65, 80, 98% for Pa γ and He I 77.9, 90.2, 96% intensity levels for O I 1.317 μm and [Fe II] 1.644 μm, 87.7, 94.9% intensity levels for [Fe III] 2.218 μm, 60, 90, 98% intensity levels for H_2 (excluding H_2 2–1 S(1), which uses 80, 90, 98% intensity levels), and the 50, 68, 85% intensity levels for the continuum at 3 μm. We note that a smoothing is applied to the [Fe III] 2.218 μm contour levels.

MIRI/MRS observations. The list is available in the science enabling products at the PDRs4All website [15]. We note that there still remain several unidentified lines in the spectra (see also Van De Putte et al. 2024).

5. Spatial variation of gas and dust tracers

Figures 7 and 8 show maps of the intensity variation of selected gas and dust tracers. Surface brightness profiles along a cut across the NIRSpec mosaic (depicted in Fig. 1, PA=155.79°) are shown in Fig. 9[16]. We discuss the Bar PDR in Sect. 5.1 and the emission associated with the two proto-planetary disks in Sect. 5.2.

5.1. Variations in the Bar

A layered structure is observed as we move away from θ^1 Ori C. The ionisation front (IF), the atomic PDR as traced by AIB emission, and the H_2 emission peak at increasing distances,

[15] https://pdrs4all.org

[16] See acknowledgments for data availability.

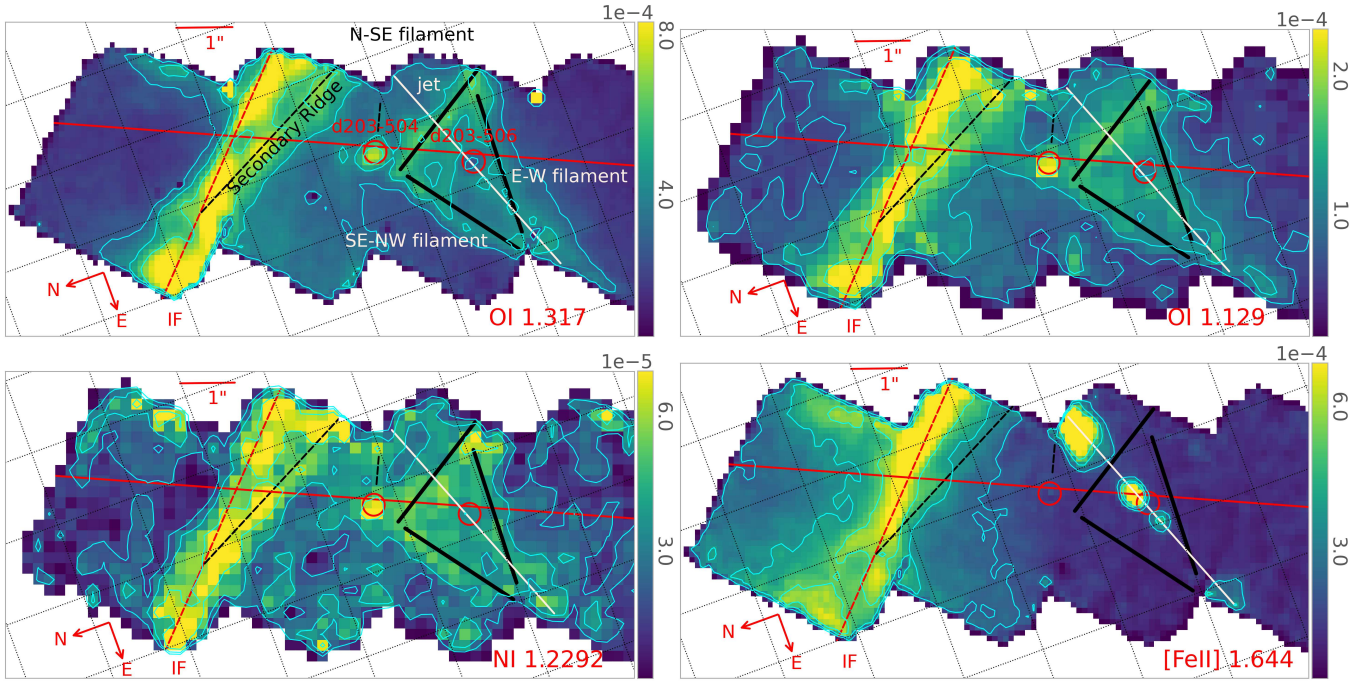

Fig. 8. Maps of O I 1.317 μm, 1.129 μm (top) as well as N I 1.2292 μm and [Fe II] 1.644 μm (bottom) across part of the NIRSpec mosaic (see the O I 1.317 μm and [Fe II] 1.644 μm maps in Fig. 7 for the full mosaic). Similar filamentary structure beyond the IF is seen in the three fluorescent lines but not in the [Fe II] 1.644 μm line. We set the colour range from the bottom 0.5% to the top 99.5% intensity levels of the data for each map (across the entire NIRSpec mosaic), excluding values of zero, edge pixels, and the two proplyds. White pixels inside the mosaic indicate values of zero reflecting issues with the data. The nearly horizontal red line indicates the NIRSpec cut and the nearly vertical red line indicates the IF. The dashed black line crossing the IF indicates the secondary ridge. The two proplyds are indicated by the circles, the jet associated with proplyd 203–504 by a white solid line and the filaments by black lines. Contours show the 77.9, 90.2, and 96% intensity levels of the data for O I 1.317 μm, 70, 85, and 97% intensity levels for O I 1.129 μm and 55, 81, and 96% intensity levels for N I 1.2292 μm, and 80, 90.2, and 96% intensity levels of the data for [Fe II] 1.644 μm (across the entire NIRSpec mosaic).

consistent with earlier studies (e.g. Tielens et al. 1993; Marconi et al. 1998; Walmsley et al. 2000; Goicoechea et al. 2015; Habart et al. 2024). However, given the angular resolution of NIRSpec, we can now observe and resolve this anatomy at sub-arcsec scales across the 0.97–5.27 μm wavelength range, which reveals filaments and ridges not seen before. For the following discussion, we define the IF by the peak intensity of the [O I] 6300 Å and [Fe II] 1.644 μm emission lines at 0.228 pc (113.4″; PA=46.21°) from θ^1 Ori C and the dissociation fronts (DFs) by the maximum intensities of the H_2 emission at 0.250, 0.257, and 0.267 pc (124.4″, 127.9″, 133.2″) from θ^1 Ori C (see below). We use the physical parameters given in Table 2 and Fig. 14 (in Sect. 6.3.2) for the different regions in the Bar.

The H I recombination lines trace the H II region. Their emission is detected throughout the mosaic, consistent with the presence of a foreground H II region in front of the atomic and molecular PDR (Fig. 14, in Sect. 6.3.2). Overall, the H I recombination lines show the same morphology. The H I emission is strongest in the H II region, peaking slightly before the IF (by 0.1″ or 0.02×10^{-2} pc) and then decreasing steeply up to $\sim 0.9 \times 10^{-2}$ pc (~4.5″) from the IF, before levelling off at longer distances. In addition to this overall morphology with distance from θ^1 Ori C, the H I emission shows structure on smaller scales in the H II region (in front of the IF) and its peak intensity near the IF is enhanced in the south-western half compared to that in the north-eastern half. Further structure is observed near the proplyds (see Sect. 5.2).

The AIB emission traces the atomic PDR. The transition from the H II to the H I region, as traced by the AIB emission, is very sharp, with a change in surface brightness of up to ~65% over a distance of ~1″. The AIB emission remains roughly constant up to $\sim 1.3 \times 10^{-2}$ pc (~6.5″) from the IF, after which it gradually decreases. It exhibits local maxima near the proplyds (Sect. 5.2). Additional local maxima are detected near the three dissociation fronts, but these maxima are slightly displaced with respect to the dissociation fronts by 0.02, 0.06, and 0.04×10^{-2} pc (0.1″, 0.3″, and 0.2″) towards the south for DF 1, DF 2, and DF 3, respectively. The AIB emission is highly structured across the atomic PDR. Specifically, the emission just past the IF is highly variable and shows additional local maxima at a distance of ~2″ from the northern part of the IF covered by the mosaic, in the S-SE direction of proplyd 203–504, and south of prolyd 203–506 (by about 0.2–1.2″). Lastly, in front of the IF, the AIB emission originating from the background face-on PDR, OMC-1, is enhanced in the eastern half of the FOV. This enhanced emission is part of a larger structure seen in the NIRCam AIB image (Fig. 1, red colour) and is not correlated with the foreground extinction (see Sect. 6.1). This suggests that the background PDR, OMC-1, displays an irregular surface that is affecting the amount of UV-excitation of the AIB carriers, as previously noted by, for example, Salgado et al. (2016).

The H_2 emission traces the dissociation fronts. The morphology of the H_2 lines (H_2 0–0 S(9), 1–0 S(1), 2–1 S(1), and 1–0 O(5) at 4.695, 2.122, 2.248, and 3.235 μm, respectively) are consistent with one another. H_2 emission is observed throughout the mosaic, with higher intensities found in the lower half of the mosaic that trace the molecular PDR. Enhanced emission is also observed in the molecular PDR at 2.21, 2.92, and 3.97×10^{-2} pc (11.03″, 14.55″, and 19.80″) from the IF, which subsequently

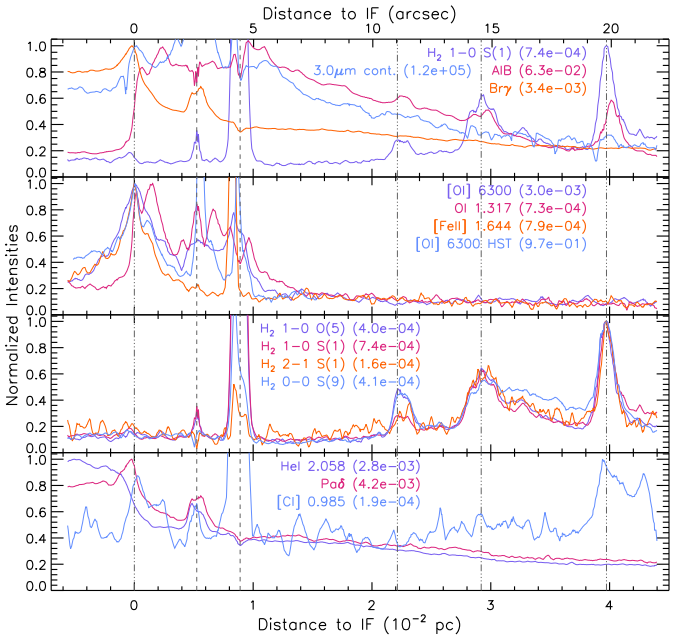

Fig. 9. Normalised line intensities as a function of distance to the IF (0.228 pc or 113.4″ from θ^1 Ori C) along a cut crossing the NIRSpec mosaic (see also Figs. 1 and 7 for the location of the cut). Normalisation factors are listed between brackets for each intensity. As the cut is not perpendicular to the IF and distances are given along the cut, a correction factor of cos(19.58°)=0.942 needs to be applied to obtain a perpendicular distance from the IF. No extinction correction is applied. For reference, we show the extinction corrected [O I] 6300 Å emission observed by Weilbacher et al. (2015) in purple and the [O I] 6300 Å emission observed by Bally et al. (2000) in light blue along the same cut. The dash-dot-dot-dot vertical lines indicate the position of the IF, DF 1, DF 2, and DF 3 respectively from left to right. The dashed vertical lines indicated the location of the proplyds 203–504 (left) and 203–506 (right). Units are erg cm^{-2} s^{-1} sr^{-1} except for the 3.0 μm continuum which is in MJy sr^{-1} and the HST [O I] 6300 Å emission which is in counts s^{-1}.

defines three dissociation fronts in the edge-on PDR. The intensity of these four H_2 lines peak at DF 3, followed by DF 2 and DF 1. Towards the northern part of the atomic PDR, we detect enhanced H_2 emission in the eastern half of the mosaic. Additionally, as for the AIB emission, in the region in front of the IF, we detect enhanced H_2 emission in the eastern half of the mosaic. We note that this emission is originating from the background face-on PDR in the molecular cloud, OMC-1.

The peak [Fe II] 1.644 μm emission is co-spatial with the peak [O I] 6300 Å emission. This is consistent with observations with MUSE by Weilbacher et al. (2015, extinction-corrected) and by HST from Bally et al. (2000, not extinction-corrected), indicating [Fe II] is an excellent tracer of the IF. The drop in [Fe II] intensity away from the IF is sharper than the drop in the MUSE [O I] 6300 Å intensity due to the lower angular resolution of the latter. The IF towards the west of the mosaic is more pronounced (i.e. larger intensity variation over a smaller area) than towards the east, consistent with the sharper transitions seen along a cut perpendicular to the bar, but west of the NIRSpec mosaic (Habart et al. 2024). On smaller spatial scales, both tracers exhibit almost identical profiles along the IF.

The [Fe III] 3.229 μm emission is detected in front of the IF and thus inside the H II region. The sharp drop in [Fe II] intensity towards θ^1 Ori C is likely caused by the transition from Fe II to predominantly Fe III in front of the IF.

The overall morphology of the He I emission lines is the same, although small differences are observed between the measured transitions (see Sect. 6.2). He I emission is observed throughout the mosaic, peaking closest to θ^1 Ori C, and displays a different spatial profile compared to that of the H I emission. Closest to θ^1 Ori C, its intensity is roughly constant or decreases slightly with distance from θ^1 Ori C. We note that the NIRSpec mosaic covers only a small part of the Huygens H II region and, thus, likely misses the real He I emission peak. Subsequently, it drops rapidly. This sudden decrease in intensity starts before the IF, where the H I intensity starts to increase. In contrast to [Fe II] and H I , this rapid drop is less sharp and already transitions to a slow steady decline at 0.15×10^{-2} pc (0.74″) after the IF.

The O I 1.317 μm emission peaks just beyond the IF and, overall, drops off sharply with increasing distance from the IF. This transition arises from O I in the neutral gas that is UV-pumped to its upper level, resulting in peak emission just beyond the IF. We do not observe enhanced emission in the direction of θ^2 Ori A (located to the east of the mosaic), suggesting that θ^1 Ori C is the main source of UV radiation. The structure seen in the [Fe II] emission along the IF is mimicked (but offset) by the O I 1.317 μm emission. The latter also exhibit a secondary, slightly weaker, ridge south of the primary ridge, at a small angle with the primary ridge (about 14 degrees), as well as enhanced emission towards the eastern edge of the IF, neither of which are prominently seen in [Fe II] or [O I] 6300 Å, albeit both show slightly enhanced emission near the peak of the secondary ridge (also offset, Fig. 8). The O I 1.317 μm emission displays filamentary structure between 3–6″ south of the IF, south of the proplyd 203–504, and surrounding the proplyd 203–506 (Fig. 8). These filaments' projections resemble a triangle with the strongest filament (N-SE filament) being parallel to the secondary ridge. These filaments are not seen in [Fe II] emission, which traces the IF. However, the SE-NW and the N-SE filaments do show weak emission in [O I] 6300 Å (Bally et al. 2000) and enhanced AIB emission is seen in part of the SE-NW filament. Two other fluorescent transitions within our wavelength coverage, the O I 1.129 μm and N I 1.2292 μm transitions, exhibit the same spatial distribution as the O I 1.317 μm emission (Fig. 8). The filamentary structure in the SE-NW direction towards proplyd 203–504 is associated with this proplyd (Sect. 5.2). While the lower half of the filamentary structure directed in the E-W direction may be aligned with the southern jet from proplyd 203–506 as seen in [Fe II], the top half is clearly offset from this jet by ∼16 degrees. We note this filament is slightly bent.

The spatial distribution of the [C I] 0.985 μm line is unique (Fig. 9): the observed variations in its intensity are only half of those seen in other tracers (excluding the proplyds) and it exhibits a 'flat' profile with local maxima just beyond the IF, and at the proplyds, DF 2, and DF 3 (though not at DF 1). We thus confirm that the C I originates in the neutral gas beyond the IF. The [C I] line shows enhancements at 2 out of the 3 H_2 dissociation fronts, similar to the results of Walmsley et al. (2000), but over a much larger distance scale. In contrast to Walmsley et al. (2000, due to their lower angular resolution), [C I] 0.985 μm exhibits a local maximum just beyond the IF (co-spatial with the double ridge seen in O I 1.317 μm), which is absent in H_2 and reflects the much smaller scale size near the IF.

Lastly, the continuum emission at 3 μm is strong in the H II region (see Figs. 7 and 9) due to the enhanced contribution of free-free emission and free-bound emission. An increase in intensity occurs near the IF, resulting in a local peak, co-spatial with the O I 1.317 μm peak emission. The continuum emission

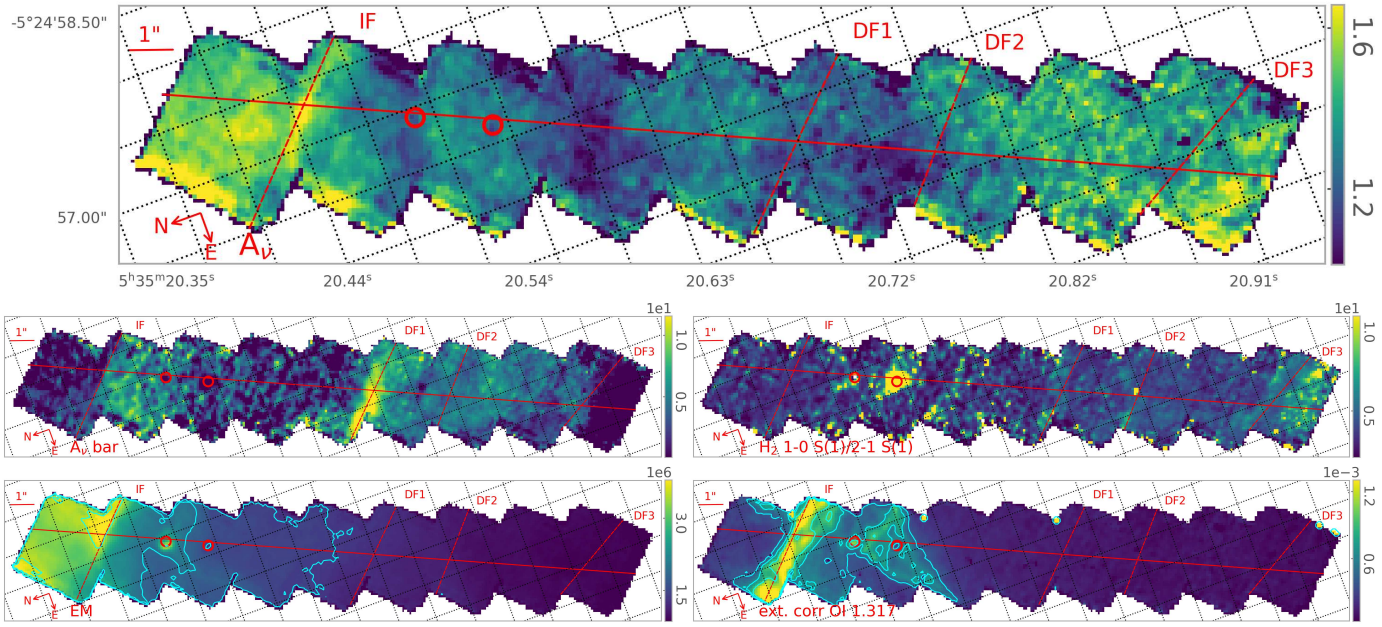

Fig. 10. Maps of the visual line of sight foreground extinction A_V (Sect. 6.1, top), the visual line of sight internal PDR extinction $A_{V_{\rm bar}}$ (Sect. 6.4, middle left), the H_2 1–0 S(1)/2–1 S(1) ratio (Sect. 6.4, midle right), the Emission Measure (EM; in units of pc cm^{-6}, Sect. 6.1, bottom left), and the extinction corrected O I 1.317 μm (ext. corr. O I 1.317 μm; in units of erg cm^{-2} s^{-1} sr^{-1}, bottom right). We set the colour range from the bottom 0.5% to the top 99.5% of data for each map, excluding values of zero, edge pixels, and the two proplyds. White pixels inside the mosaic indicate values of zero reflecting issues with the data. The nearly horizontal red line indicates the NIRSpec cut and the nearly vertical red lines indicate from left to right the IF and the DFs (DF 1, DF 2, DF 3). The two proplyds are indicated by the circles. Contours show the 55, 78, and 98% of the data for EM, and 77.9, 90.2, and 96 for O I 1.317 μm (see acknowledgments for data availability).

remains strong throughout the atomic PDR and displays small-scale variations that mimic those seen in the AIB emission (see also Appendix C). This indicates that the continuum emission in the PDR is dominated by emission from stochastically heated very small grains and/or by blended overtone and combination bands of PAHs, consistent with previous reports (Sellgren 1984; Allamandola et al. 1989). In addition, very strong continuum emission is detected towards the proplyd 203–504[17]. The continuum emission slowly decreases deeper into the molecular PDR due to the geometrical dilution of the radiation field.

5.2. Variations in protoplanetary disks

Two proto-planetary disks are present within the NIRSpec mosaic: the bright proplyd 203–504 and the silhouette disk 203–506 (Fig. 1, Bally et al. 2000). The 203–504 proplyd shows strong emission from H I recombination lines, He I, the fluorescent O I and N I lines, [C I] 0.985 μm, and H_2, and enhanced AIB emission. A filamentary structure starting at this proplyd and extending towards the SE direction is seen in the H I recombination lines. This SE-NW filament has been reported by Bally et al. (2000) in Hα and [O I] 6300 Å, being identified as a monopolar jet associated with the proplyd. The fluorescent lines also show a filamentary structure associated with this jet, but while this emission is parallel to the filament seen in H I , it is offset to the west by ∼0.2″. No enhanced [Fe II] emission is observed in this filament. Enhanced emission in the H I recombination lines is also seen towards the SSW of the proplyd.

The proplyd 203–506 is discussed in detail by Berné et al. (2024) and Berné et al. (2023). In addition to these authors' results, we report that the proplyd exhibits strong emission in [O I] 6300 Å and [C I] 0.985, and the disk is seen in absorption in He I and the fluorescent O I and N I lines. The [Fe II] emission is bright perpendicularly to the major axis of the silhouette disk 203–506, and on both sides, tracing the launching zone of a faint collimated jet observed before in [O I] 6300 Å HST images (Bally et al. 2000). Extending in the jet direction, towards the north-west and south-east, we observe enhanced [Fe II] emission, with the north-west component being much brighter than the south-east component. This is suggestive of a Herbig-Haro object being associated with the proplyd jet.

6. Deriving physical parameters

6.1. H I recombination lines

The H I recombination lines provide an estimate of the foreground extinction by comparing the observed ratios with those from case B recombination theory assuming an electron temperature of 10 000 K[18], an electron density of n_e = 1000 cm^{-3} and no radiation field (Prozesky & Smits 2018). We use the ratio of Paschen δ and Brackett γ. Both lines are among the strongest H I lines observed with detector NRS1 and have a large wavelength difference. We adopt the NIR extinction curve from Gordon et al. (2023) for an R_V = 5.5 (Cardelli et al. 1989). The resulting foreground visual extinction, A_V, varies between roughly 0.9 and 1.9 magnitude, corresponding to c(Hβ)[19]

[17] The 'extended' 3 μm continuum emission near proplyd 203–504 are the wings of the point spread function (PSF).

[18] Here we have adopted an electron temperature for our analysis of 10 000 K. Adopting a temperature instead of 9000 K (8500 K) would increase the theoretical Br γ/Pa δ line ratio by ∼1.4% (2.2%) resulting in an average decrease in A_V of 3.5% (5.2%).

[19] c(Hβ) = log($\frac{I_{0,H\beta}}{I_{\rm obs,H\beta}}$) with $I_{0,H\beta}$ the surface brightness in the absence of extinction and $I_{\rm obs,H\beta}$ the observed surface brightness.

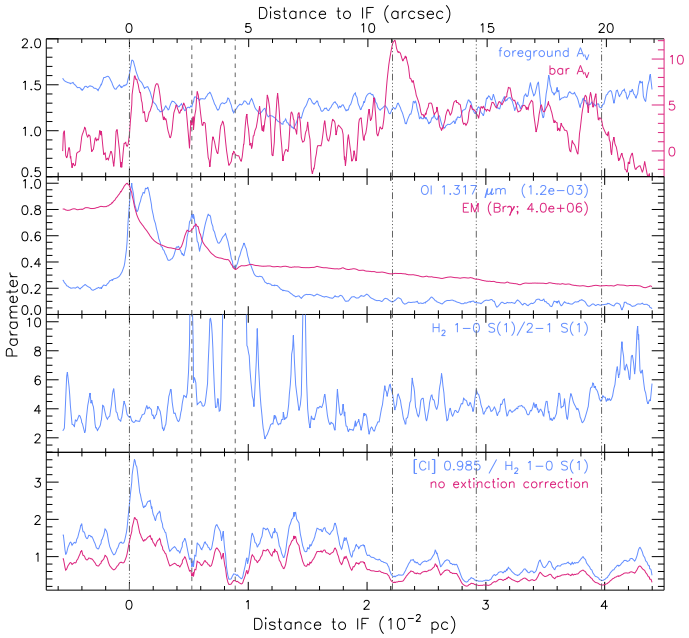

Fig. 11. Foreground extinction (top panel, left y-axis), internal PDR extinction (top panel, right y-axis), normalised O I 1.317 μm line intensity and emission measure (second panel), and line intensity ratios (lower two panels) as a function of distance to the IF (0.228 pc or 113.4″ from θ^1 Ori C) along a cut crossing the NIRSpec mosaic (see Fig. 1). Normalisation factors are listed between brackets where applied. As the cut is not perpendicular to the IF and distances are given along the cut, a correction factor of cos(19.58°)=0.942 needs to be applied to obtain a perpendicular distance from the IF. Foreground extinction correction is applied to determine bar A_V ($A_{V_{\rm bar}}$) and for the line intensities and ratios depicted in blue colour. The dash-dot-dot-dot vertical lines indicate the position of the IF, DF 1, DF 2, and DF 3 respectively from left to right. The dashed vertical lines indicated the location of the proplyds 203–504 (left) and 203–506 (right) (see acknowledgments for data availability).

of 0.4–0.8 when using the extinction curve of Blagrave et al. (2007, Figs. 10 and 11). To first order, the derived foreground extinction decreases slightly with distance from θ^1 Ori C up to about a distance of $\sim 2.6 \times 10^{-2}$ pc (~13″) from the IF, after which it slowly increases. It is also slightly structured, with weak local minima near, roughly, 0.4, 1.4, and 2.6×10^{-2} pc (~2″, ~7″, and ~13″) from the IF. The derived extinction values are overall consistent with Weilbacher et al. (2015), but the morphology differs slightly. Specifically, neither the increase in the extinction past roughly $\sim 2.6 \times 10^{-2}$ pc (~13″) from the IF nor the local minima are observed by Weilbacher et al. (2015). In addition, Weilbacher et al. (2015) derived a slightly increased extinction at the western side of the NIRSpec mosaic in the atomic PDR. These discrepancies likely results from the combination of 1) the lower angular resolution observations of Weilbacher et al. (2015, seeing of 0.67″ to 1.25″) resulting in a spatial averaging weighted by the emissivities, and 2) remaining systematic artefacts in the data set that are not captured by the comparison of these line fluxes in the individual dither observations (which agree within 0.5%).

A caveat of the presented extinction analysis is the following. The extinction is a summation of absorption and scattering out of the line of sight. For the Bar, we have an extended background light source and the extinction is due to foreground extended dust. If the background light source and dust layer are both uniformly distributed, the light scattered outside the line of sight will be compensated by the light scattered in the line of sight for a spherically symmetric, unresolved source. Therefore, the net attenuation will only be due to absorption. However, the actual situation is more complex. Both the background light source and the dust are distributed heterogeneously and it is impossible to estimate the actual geometry. But in general, the attenuation will be reduced by the light scattered into the line of sight (cf. Code 1973). While the general trend of the determined extinction, A_V, should not be affected very much, it does affect the quantitative value of A_V obtained from the standard extinction curve, which is estimated from observations of background stars. As the albedo is still around ~0.5 in the NIR, the absorption will only be a half of extinction. The spectral dependence is also different between the absorption and scattering. However, this should not make a large difference because of the short spectral range considered and small attenuation in question. Despite this caveat, we use these derived values for the foreground extinction to the Bar and employ the NIR extinction curve for an $R_V = 5.5$ from Gordon et al. (2023)[20].

WeAs obtain an estimate of the emission measure, EM, from the Brackett γ surface brightness using Eq. (D.1). The emission measure ranges within $0.84–4.15 \times 10^6$ pc cm^{-6} (Figs. 10 and 11; see Table 1 for the five templates). The obtained EM in front of, and at the IF are consistent with those reported by Walmsley et al. (2000) for similar regions north-east of the NIRSpec mosaic (their positions A and B). Assuming a depth of the ionised bar of 20″ (0.05 pc; Walmsley et al. 2000), we obtain a rms electron density of the order of 9000 cm^{-3}.

6.2. HeI recombination lines

The distinct radial profiles for the He I and H I recombination lines (Figs. 9 and 12) indicate, for the first time, that the He and H ionisation fronts are clearly separated in the Huygens region. While the location of the H-IF is well defined (i.e. peak H I emission at 0.2274 pc or 113.276″ from θ^1 Ori C), the location of the He-IF is somewhat uncertain as the NIRSpec radial profiles do not extend very deep into the Huygens region. However, the He I 1.70 μm intensity remains fairly constant up to about 15″ away from the IF (Marconi et al. 1998). Hence, we quantify the displacement between the H-IF and He-IF by the distance between the peak emission of the H I and He I recombination lines and find a displacement of approximately 0.5×10^{-2} pc or 2.5″ (Fig. 12). Only the He I 1.083 μm emission gives a slightly smaller displacement of 0.36×10^{-2} pc (1.8″).

These results are consistent with Cloudy modelling (Ferland et al. 2017) of the Orion Nebula. We adopt the model parameters derived from the detailed fits of the optical lines originating from the ionised gas by Shaw et al. (2009) and Pellegrini et al. (2009)[21]. In a radial direction from θ^1 Ori C, this model predicts the H IF at a distance of ~0.254 pc and a displacement between

[20] This extinction curve has A_λ/A_V values of 5.075×10^{-1}, 2.711×10^{-1}, 1.736×10^{-1}, 1.258×10^{-1}, 9.838×10^{-2}, 7.995×10^{-2}, 6.695×10^{-2}, 5.747×10^{-2}, and 5.037×10^{-2} at 1.0, 1.5, 2.0, 2.5, 3.0, 3.5, 4.0, 4.5, and 5.0 μm respectively and 1.508×10^{-1} at 2.2 μm.

[21] It should be noted that the analysis from Shaw et al. (2009) and Pellegrini et al. (2009) required the models to reproduce the projected distance of the IF, which was defined based on the peak emission of [S II] at a projected distance from θ^1 Ori C of 111″. These authors adopt a distance of 437 pc for the Bar and thus the IF is located at a projected distance of 0.235 pc. In this paper, we instead define the IF by the peak intensity of the [O I] 6300 Å and [Fe II] 1.644 μm emission lines at 113.4″ or 0.228 pc from θ^1 Ori C (given the adopted distance of 414 pc). This small difference should, however, not considerably affect the spatial offset between the He and H ionisation front.

Table 1. Physical conditions derived for the five templates.

		Sect.	H II region	Atomic PDR	DF 1	DF 2	DF 3
A_V [(1)]		6.1	1.5	1.3	1.2	1.2	1.4
$A_{V_{\rm bar}}$ [(2)]		6.4	–	2.84	8.55	3.67	1.28
$A_{V_{\rm bar},I}$ [(3)]		6.4	0	5.49	36.1	7.44	2.30
EM (Brγ)	(10^6 pc cm^{-6})	6.1	3.3	2.3	1.2	1.1	0.9
T (C I)	(K)	6.5, G	~2500	~2300	~2900	~6800	~5600
EM×$T_3^{-0.6}$ (C I)	(cm^{-6} pc K$^{-0.6}$)	6.5, G	1034±18	2635±40	725±11	938±15	1589±17
EM (C I)	(pc cm^{-6})	6.5, G	1772^{+247}_{-240}	4334^{+602}_{-539}	1370^{+451}_{-401}	2953^{+790}_{-576}	4477^{+472}_{-350}
3.4/3.29 AIB [(4)]		6.6.1	0.11	0.09	0.10	0.15	0.18
4.64/ΣAIB [(5)]	(10^{-3})	6.6.1	8.2	6.3	6.1	2.8	2.4
4.64/3.29 AIB	(10^{-3})	6.6.1	16.0	12.1	11.9	6.0	5.6
4.64/3.40 AIB	(10^{-2})	6.6.1	20.5	22.5	15.8	5.4	4.1
FWHM 3.29 AIB	(cm^{-1})	6.6.2	39.3	37.4	38.1	41.2	42.4

Notes. We provide the H_2 excitation temperatures and column densities in Table 4. [(1)]foreground extinction; [(2)]internal PDR extinction calculated using the foreground formalism (see Fig. 14); [(3)]internal PDR extinction calculated using the intermingled formalism; [(4)]ratio of the integrated intensities of the (3.39+3.40+3.42)/(3.29) AIBs using the Gaussian decomposition method. [(5)]ΣAIB refers to the sum of all Gaussian AIB components in the 3.2–3.7 μm range.

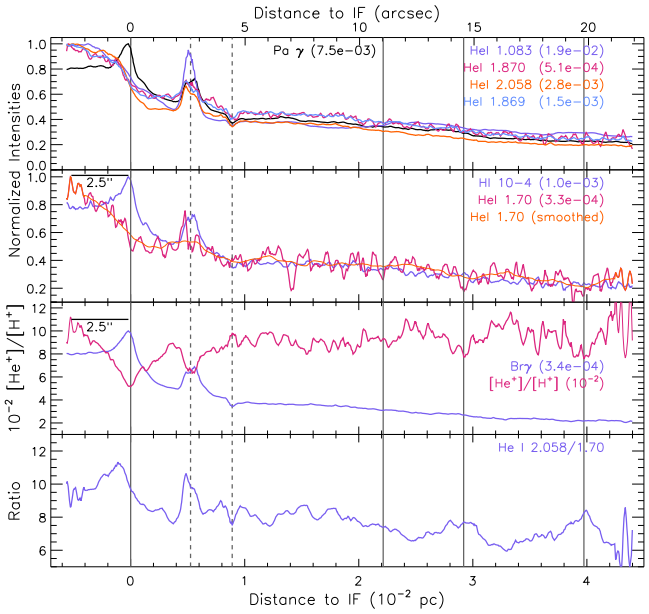

Fig. 12. Analysis of the He I and H I radial profiles as a function of distance to the IF (0.228 pc or 113.4″ from θ^1 Ori C) along a cut crossing the NIRSpec mosaic (see Fig. 1). As the cut is not perpendicular to the IF and distances are given along the cut, a correction factor of cos(19.58°)=0.942 needs to be applied to obtain a perpendicular distance from the IF. Top two panels: observed normalised line intensities of selected transitions. Normalisation factors are listed between brackets. No extinction correction is applied. Units are in erg cm^{-2} s^{-1} sr^{-1}. Third panel: the [He$^+$]/[H$^+$] abundance. The normalised Br γ radial profile is shown for reference. Normalisation factors are listed between brackets. Bottom panel: the He I 2.058/1.70 radial profile. The dash-dot-dot-dot vertical lines indicate the position of the IF, DF 1, DF 2, and DF 3, respectively, from left to right. The dashed vertical lines indicated the location of the proplyds 203–504 (left) and 203–506 (right).

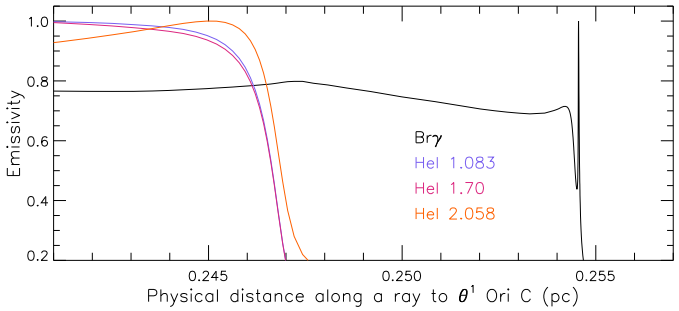

Fig. 13. Emissivity profile of selected transitions as a function of the physical distance along a ray from θ^1 Ori C and perpendicular to the Bar given by a Cloudy model employing the physical parameters derived by Shaw et al. (2009) and Pellegrini et al. (2009). See Sect. 6.2 for details.

the emissivity of selected H and He transitions of ~0.007 pc (Fig. 13). We note that the latter distances are physical distances along a ray into, and perpendicular to, the Bar from θ^1 Ori C as we did not model the corresponding radial surface brightness profiles of selected transitions as a function of the projected distance from θ^1 Ori C. These differences result in an offset between the model IF and our observations. We conclude therefore that the model calculations are in good agreement with the He I and H I observations reported here.

Based on the radial profiles of He I 1.70 μm and H I 10-4, we can estimate the [He$^+$]/[H$^+$] abundance following Marconi et al. (1998, see Appendix E). Figure 12 shows the radial profile along the NIRSpec cut. Over most of the radial profile, the [He$^+$]/[H$^+$] abundance is fairly constant. However, due to NIRSpec's angular resolution, we also detect two strong dips. The dip at the IF reflects the displacement of the H-IF and He-IF, while the second dip is co-spatial with the proplyd 203–504. We note that the He I emission near this proplyd depends on the transition considered. Away from the IF and this proplyd, we derive a [He$^+$]/[H$^+$] abundance of 0.094 ± 0.009. While previous observations did not resolve the difference in the H and He ionisation structure in the Huygens region, these studies obtain a similar [He$^+$]/[H$^+$] abundance because of spatial averaging (e.g. Osterbrock et al. 1992; Esteban et al. 1998, 1994; Marconi et al. 1998; Baldwin et al. 2000; Walmsley et al. 2000; Blagrave et al. 2007). Recent refinements in the atomic data